The Astrophysical Journal, 962:88 (31pp), 2024 February 10 https://doi.org/10.3847/1538-4357/ad1387

The EDGE-CALIFA Survey: Molecular Gas and Star Formation Activity across the Green Valley

Vicente Villanueva[1,2,12], Alberto D. Bolatto[1], Stuart N. Vogel[1], Tony Wong[3], Adam K. Leroy[4,5], Sebastian F. Sánchez[6], Rebecca C. Levy[7,13], Erik Rosolowsky[8], Dario Colombo[9], Veselina Kalinova[10], Serena Cronin[1], Peter Teuben[1], Mónica Rubio[11], and Zein Bazzi[9]
[1] Department of Astronomy, University of Maryland, College Park, MD 20742, USA; vvillanu@umd.edu
[2] Departamento de Astronomía, Universidad de Concepción, Barrio Universitario, Concepción, Chile
[3] Department of Astronomy, University of Illinois, Urbana, IL 61801, USA
[4] Department of Astronomy, The Ohio State University, Columbus, OH 43210, USA
[5] Center for Cosmology and Astroparticle Physics, 191 West Woodruff Avenue, Columbus, OH 43210, USA
[6] Instituto de Astronomía, Universidad Nacional Autónoma de México, A.P. 70-264, 04510 México, D.F., Mexico
[7] Steward Observatory, University of Arizona, Tucson, AZ 85721, USA
[8] Department of Physics, University of Alberta, 4-181 CCIS, Edmonton, AB T6G 2E1, Canada
[9] Argelander-Institut für Astronomie, Universität Bonn, Auf dem Hügel 71, D-53121 Bonn, Germany
[10] Max Planck Institute for Radioastronomy, Auf dem Hügel 69, D-53121, Bonn, Germany
[11] Departamento de Astronomía, Universidad de Chile, Casilla 36-D Santiago, Chile
Received 2023 September 6; revised 2023 November 17; accepted 2023 December 6; published 2024 February 8

Abstract

We present a ^{12}CO($J = 2-1$) survey of 60 local galaxies using data from the Atacama Compact Array as part of the Extragalactic Database for Galaxy Evolution: the ACA EDGE survey. These galaxies all have integral field spectroscopy from the CALIFA survey. Compared to other local galaxy surveys, ACA EDGE is designed to mitigate selection effects based on CO brightness and morphological type. Of the 60 galaxies in ACA EDGE, 36 are on the star formation main sequence, 13 are on the red sequence, and 11 lie in the "green valley" transition between these sequences. We test how star formation quenching processes affect the star formation rate (SFR) per unit molecular gas mass, $\mathrm{SFE_{mol}} = \mathrm{SFR}/M_{\mathrm{mol}}$, and related quantities in galaxies with stellar masses $10 \leqslant \log[M_\star/M_\odot] \leqslant 11.5$ covering the full range of morphological types. We observe a systematic decrease of the molecular-to-stellar mass fraction ($R_\star^{\mathrm{mol}}$) with a decreasing level of star formation activity, with green valley galaxies also having lower $\mathrm{SFE_{mol}}$ than galaxies on the main sequence. On average, we find that the spatially resolved $\mathrm{SFE_{mol}}$ within the bulge region of green valley galaxies is lower than in the bulges of main-sequence galaxies if we adopt a constant CO-to-H_2 conversion factor, α_{CO}. While efficiencies in main-sequence galaxies remain almost constant with galactocentric radius, in green valley galaxies, we note a systematic increase of $\mathrm{SFE_{mol}}$, $R_\star^{\mathrm{mol}}$, and specific SFR with increasing radius. As shown in previous studies, our results suggest that although gas depletion (or removal) seems to be the most important driver of the star formation quenching in galaxies transiting through the green valley, a reduction in star formation efficiency is also required during this stage.

Unified Astronomy Thesaurus concepts: Extragalactic astronomy (506)

1. Introduction

Star formation activity plays a key role in driving the growth and evolution of galaxies. The production of stars is quantified through the star formation rate (SFR), which is, in principle, a function of the physical conditions in the dense interstellar medium (ISM). In the last few decades, several studies have revealed a tight correlation for many galaxies between the integrated SFR and the stellar mass ($M_\star$) in galaxies, the so-called star formation main sequence (SFMS; e.g., Brinchmann et al. 2004; Daddi et al. 2007; Whitaker et al. 2012; Saintonge et al. 2016; Colombo et al. 2020). This implies a useful galaxy classification in terms of their star formation status: "blue cloud" galaxies, which show a direct correlation between $M_\star$ and SFR for active star-forming (SF) galaxies; "red cloud," where galaxies exhibit low SFRs and no $M_\star$–SFR correlation; and the "green valley" (or transition galaxies; Salim et al. 2007). The bimodality of the SFMS suggests fundamental questions regarding the physical processes behind the transition from the SFMS through the green valley and the red cloud, which is mostly linked to the cessation of star formation activity.

The term "quenching" has been adopted to include the variety of mechanisms behind the cessation of star formation activity in galaxies. In particular, Peng et al. (2010) suggest two different routes to classify quenching processes: "environmental quenching," which is coupled to the local environmental conditions that may drive the decrease (or cessation) of SFR, and "mass quenching," which refers to internal/intrinsic galaxy mechanisms affecting star formation. While environmental processes mostly take place in galaxies residing in high-density environments (e.g., galaxy clusters) encompassing a broad variety of environmental mechanisms (e.g., strangulation/starvation, Larson et al. 1980; Balogh & Morris 2000; ram pressure stripping, Gunn & Gott 1972; galaxy interactions,

[12] ALMA-ANID Postdoctoral Fellow.
[13] NSF Astronomy and Astrophysics Postdoctoral Fellow.

Moore et al. 1996; Smith et al. 2010), intrinsic mechanisms are usually associated with the activation and regulation of the physical processes driving star formation activity. Intrinsic quenching mechanisms are also expected to act differently depending on the structural components within galaxies, resulting in variations in the SFR when comparing bulges, bars, or disks. These intrinsic mechanisms have been broadly associated with fast quenching processes ($\lesssim$100 Myr; e.g., Bluck et al. 2020b, 2020a) or slow aging ($\sim$0.5–1 Gyr; e.g., Corcho-Caballero et al. 2023), which act in different ways to alter the physical conditions of the gas and span from strangulation (i.e., star formation continues until the reservoirs of cold gas are depleted; e.g., Kawata & Mulchaey 2008; Peng et al. 2015) to gas removal, either due to active galactic nuclei (AGN) suppression (e.g., Oppenheimer et al. 2010; Page et al. 2012) or via stellar feedback (e.g., supernova winds; Oppenheimer et al. 2010).

Recent theoretical models have shown that some of these intrinsic mechanisms rely on modifying the physical properties of the ISM, thereby changing the efficiency by which the molecular gas is transformed into stars. Martig et al. (2009) proposed "morphological quenching," a process in which star formation is suppressed by the formation of a stellar spheroid. According to Martig et al. (2009), morphological quenching reflects the stabilization of the disk by the dominant presence of a pressure-supported stellar spheroid, which replaces the stellar disk. The stabilization of the gas is a consequence of two effects: (i) the steep potential well induced by the spheroid and (ii) the increase of a stellar spheroid relative to the stellar disk suppressing the growth of perturbations in the gaseous disk. This process provides a mechanism through which early-type galaxies (ETGs) lose their ability to form stars even in the presence of significant cold gas reservoirs (e.g., Martig et al. 2013). Gravitational instability is key to increasing the SFR. In a simple model, stability is typically estimated by the Toomre Q parameter, $Q = \frac{\kappa\sigma}{\epsilon_{\rm f} G\Sigma}$ (Toomre 1964), where σ is the one-dimensional dispersion velocity of the gas, $\sigma_{\rm gas}$; Σ is the surface density of an infinitely thin disk; and κ is the epicyclic frequency, which is linked to the steepness of the gravitational potential and is of order the angular velocity Ω. Axisymmetric instabilities, which create rings that break up into clouds, can grow in the disks if $Q < 1$. Martig et al. (2009) suggested that morphological quenching is the severe suppression of star formation activity in a massive gaseous disk when it is embedded in a dominant bulge that stabilizes the gas (i.e., resulting in $Q \gg 1$). When compared with the star formation activity in spirals, the difference in disk stability in ETGs arises from two main effects: (i) the high central concentration of the stellar mass in ETGs increases κ, consequently increasing the tidal forces as well, and (ii) the spheroidal distribution of stars dilutes the self-gravity of the gas, and therefore gravitational collapse cannot counteract the tidal forces, preventing the assembly of SF clumps. Also through numerical simulations, Gensior et al. (2020) show that spheroids drive turbulence and increase $\sigma_{\rm gas}$, increase the virial parameter, and cause the turbulent pressure to increase toward a galaxy center; all these are mostly dependent on the bulge mass ($M_{\rm b}$). They also find that turbulence increases for more compact and more massive bulges. Although morphological quenching is a process able to reduce the star formation during a well-defined time range of a galaxy lifetime ($t \approx$7–11 Gyr; Martig et al. 2009), it is still not clear to what degree the aging in ETGs is driven by this mechanism, the reduction of the molecular gas content, or a combination of multiple processes.

By obtaining high-resolution CO data, the new generation of millimeter/submillimeter telescopes has allowed us to analyze in detail how the physical conditions of the molecular gas vary between the different structural components within galaxies in the local Universe. In addition, multiwavelength galaxy surveys have revealed the interplay between the different components of the ISM and their role in star formation activity. In this work, we present the Atacama Compact Array Extragalactic Database for Galaxy Evolution, the ACA EDGE survey. We investigate the star formation activity in 60 nearby massive galaxies using ACA observations of the CO(2−1) emission line in combination with optical integrated field unit (IFU) data from the Calar Alto Legacy Integral Field Area (CALIFA) survey (Sánchez et al. 2012).

This paper is organized as follows. Section 2 presents the main features of the ACA EDGE survey, including the sample selection, data processing, and ancillary data. In Section 3, we explain the methods applied to analyze the data and the equations used to derive the physical quantities. Finally, in Section 4, we present our results and discussion, and in Section 5, we summarize the main conclusions. Throughout this work, we assume a ΛCDM cosmology, adopting the values $\Omega_\Lambda = 0.7$, $\Omega_{\rm DM} = 0.3$, and $H_0 = 69.7\ {\rm km\ s^{-1}\ Mpc^{-1}}$.

2. Observations

2.1. The ACA EDGE Sample

We used the ACA to observe 60 galaxies drawn from the CALIFA survey Data Release 3 (Sánchez et al. 2016a) in the context of the EDGE surveys. Previous CO surveys focus mainly (or exclusively) on "main-sequence" or SF galaxies selected due to either their SFR/$M_\star$, morphology, or IR brightness (e.g., the HERA CO Line Extragalactic Survey, HERACLES, Leroy et al. 2008, 2013; the Herschel Reference Survey, Boselli et al. 2010; the James Clerk Maxwell Telescope Nearby Galaxies Legacy Survey, Wilson et al. 2012; the CO Legacy Database for GALEX Arecibo SDSS Survey, COLD GASS, and extended COLD GASS, Saintonge et al. 2011, 2017; the EDGE-CALIFA survey, Bolatto et al. 2017; the Virgo Environment Traced in CO survey, VERTICO, Brown et al. 2021; and the Physics at High Angular resolution in Nearby Galaxies–ALMA survey, PHANGS–ALMA, Leroy et al. 2021b). ACA EDGE was designed to probe into the low SFR/$M_\star$ regime to study processes associated with galaxy quenching. CALIFA observed over 800 galaxies with IFU spectroscopy at Calar Alto selected from a combination of the Sloan Digital Sky Survey (SDSS; York et al. 2000; Alam et al. 2015) and an extension of galaxies that fulfilled the observational setup (see Sánchez et al. 2016a for more details), reflecting the $z = 0$ galaxy population with $\log[M_\star/M_\odot] =$ 9–11.5 in a statistically meaningful manner (Walcher et al. 2014). ACA EDGE targets a subsample of CALIFA galaxies with decl. appropriate to observe with the Atacama Large Millimeter/submillimeter Array (ALMA; $\delta < 30°$) and stellar mass $M_\star > 10^{10} M_\odot$, so that CO can be readily detected and metallicity effects are not too severe. We impose no selection on SFR in order to cover the full range of star formation activities in this mass range and enable the study of quenching. The ACA EDGE survey complements the main science goals of the CARMA EDGE survey (Bolatto et al. 2017, galaxies

also drawn from CALIFA; see Figure 1), which encompasses CO observations for 126 CALIFA galaxies at ∼4.″5 resolution but with significant biases. Although CARMA EDGE-selected galaxies cover a broader range of masses ($\log[M_\star/M_\odot] = 9.1$–$11.5$), they mostly focused on late-type, far-IR detected galaxies that are rich in molecular gas (hence actively SF), with morphological types mainly spanning from Sa to Scd. The ACA EDGE survey was designed to complement it by increasing the coverage of ETGs, thus adding more red cloud galaxies to CARMA EDGE in order to drive more statistically significant results. A total of 60 galaxies were observed in CO(2–1) by the ALMA Cycle 7 project 2019.2.00029.S (PI: A. D. Bolatto). The galaxies are listed in Table 1; SDSS images are shown in Figure 2. Optical inclinations and east-of-north position angles (PAs) are taken from HyperLEDA[14] and recomputed (when applicable) using fits files from SDSS z-band photometry (see Section 3.1).

2.2. The CO Data

CO observations of our ACA-only project were taken between 2019 December and 2021 September, spending between 15 and 43 minutes on-source for each galaxy. We set a spectral bandwidth of ≈1980 MHz and a raw spectral resolution of ∼1.938 MHz ≈ 2.5 km s^{-1}. The scheduling blocks were designed to detect the CO(2−1) emission line down to an rms spanning from ∼12 to 18 mK at a 10 km s^{-1} channel width (corresponding to a mass surface density of ∼0.9–1.2 $M_\odot$ pc^{-2}) and from ∼5″ to 7″ angular resolution (i.e., probing physical scales of ∼1.5 kpc at the distance of the ACA EDGE galaxies), depending on the decl. of the source.

Each galaxy was observed in a Nyquist-spaced mosaic (between 10 and 14 pointings) aligned with the major axis, covering the source out to r_{25}. As mentioned in the previous section, we obtained 7 m ACA observations for 60, with a field of view (FoV) of ∼1.′2. Finally, we obtain 5σ CO detections for 46 ACA EDGE galaxies, giving a detection rate of ∼77%.

2.3. Data Reduction and Products

We used *uv* data delivered by ALMA and calibrated by the observatory pipeline (Hunter et al. 2023), then we imaged the CO ($J = 21$) emission from each target using the PHANGS–ALMA Imaging Pipeline version 2.1 (Leroy et al. 2021a). Both the calibration and imaging utilized the Common Astronomy Software Applications (CASA; CASA Team et al. 2022). The data were calibrated in CASA 5.6.1-8 for data taken in 2019 and 2020 and CASA 6.2.1-7 for data taken in 2021. We ran the PHANGS–ALMA imaging pipeline in CASA version 5.6.1-8.

Briefly, the PHANGS–ALMA imaging pipeline is designed to produce accurate images of extended spectral line emission. The pipeline combines all *uv* data for a given target on a common spectral grid, subtracts continuum emission, and then carries out a multistep deconvolution. This includes an initial multiscale clean (we used scales of 0″, 5″, and 10″) with a relatively high signal-to-noise ratio (S/N) of ≈4 threshold, followed by a single scale clean that uses an automatically generated, more restrictive clean mask and cleans down to S/N ≈ 1 by default. We used a Briggs weighting parameter of =0.5 (Briggs 1995) to achieve a good compromise between the synthesized beam size and S/N. We used a channel width of 5.08 km s^{-1} and adopted the local standard of rest as our velocity reference frame, using the radio definition of velocity. After the initial imaging, the pipeline convolves the cube to have a round synthesized beam, converts the image to units of kelvin, and downsamples the pixel gridding to save space while still Nyquist sampling the beam. See Leroy et al. (2021a) for more details. We did not use the noise modeling or product creation portions of the PHANGS–ALMA pipeline but instead used software based on previous EDGE work.

All cubes were visually inspected for obvious problems or imaging errors. We note that NGC 0768, NGC 6427, NGC 7321, and UGC 12250 have incomplete CO line coverage, since their emission peaks are located at the edge of the ACA spectral window. Although these galaxies have 5σ CO detections (see Section 4.1), the CO line emission flux should just be taken as lower limits.

We calculate moment maps and radial profiles using a masked cube. The construction of our mask follows a two-step procedure. We first create a mask using the CO cube, following the procedure for a "dilated mask" detailed in Bolatto et al. (2017). This procedure includes the mask areas around spectral peaks detected at ≳3.5σ significance (for more details, see Rosolowsky & Leroy 2006; Bolatto et al. 2017). We put together a second mask using information that is independent of the CO cube. We then use three different procedures to generate this mask and choose the one that recovers the most CO emission flux. These procedures are as follows.

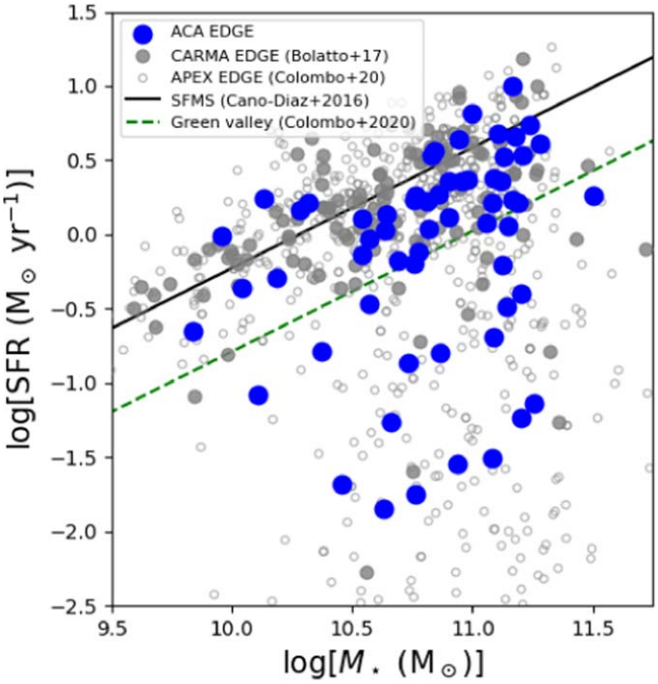

Figure 1. SFR–$M_\star$ relation for the 60 galaxies in the ACA EDGE survey (blue circles), sampling the whole range of $z = 0$ galaxy behavior for $\log[M_*/M_\odot] \approx 10$–$11.5$, including the SFMS and quenched systems below it. Gray filled and open circles are CARMA EDGE and APEX EDGE galaxies included in Bolatto et al. (2017) and Colombo et al. (2020), respectively. The black solid and green dashed lines correspond to the best linear fit for SFMS (Cano-Díaz et al. 2016) and green valley (Colombo et al. 2020) galaxies, respectively. ACA EDGE galaxies constitute a sample of the local Universe with good statistical characteristics and are easy to volume-correct to characterize the star formation activity in nearby massive galaxies.

[14] https://leda.univ-lyon1.fr/

Table 1
The ACA EDGE Target Sample

Name	R.A. (J2000)	Decl. (J2000)	i	PA	Redshift	rms	θ_{min}	θ_{maj}	PA_{beam}	Distance	R_e	r_{25}
(1)	(2)	(3)	(deg) (4)	(deg) (5)	(6)	(mK) (7)	(arcsec) (8)	(arcsec) (9)	(deg) (10)	(Mpc) (11)	(arcsec) (12)	(arcsec) (13)
CGCG 429-012	$22^h36^m49\overset{s}{.}8$	14°23′13.″1	60	4*	0.01751	12	5.3	9.7	−36.0	84	5.3	25.0
IC 1079	$14^h56^m36\overset{s}{.}1$	09°22′11.″1	50	81*	0.02907	16	6.3	7.7	−83.0	114	19.3	43.4
IC 1528	$00^h05^m05\overset{s}{.}3$	07°05′36.″3	70	72*	0.01250	13	4.6	8.2	−77.0	48	16.9	64.1
IC 2341	$08^h23^m41\overset{s}{.}4$	21°26′05.″5	60	2*	0.01701	18	6.2	8.0	−72.0	75	8.0	35.2
MCG-01-01-012	$23^h59^m10\overset{s}{.}8$	04°11′30.″6	90	70*	0.01883	13	4.4	8.1	89.0	78	11.2	47.5
MCG-01-10-015	$03^h38^m39\overset{s}{.}1$	05°20′50.″4	73	75*	0.01343	12	5.1	8.3	−48.0	90	11.8	43.4
MCG-01-52-012	$20^h37^m49\overset{s}{.}9$	06°05′26.″7	43	72*	0.01270	14	5.0	8.4	−45.0	100	4.5	35.2
MCG-02-02-030	$00^h30^m07\overset{s}{.}3$	11°06′49.″1	70	170*	0.01179	13	4.4	8.3	−76.0	42	13.9	55.9
MCG-02-51-004	$20^h15^m39\overset{s}{.}8$	13°37′19.″3	68	159*	0.01876	12	5.2	8.1	−43.0	90	15.8	45.4
NGC 0001	$00^h07^m15\overset{s}{.}8$	27°42′29.″7	34	110*	0.01511	15	4.9	11.7	−24.0	74	9.2	47.5
NGC 0155	$00^h34^m40\overset{s}{.}0$	10°45′59.″4	40	169*	0.02053	13	5.1	7.9	−47.0	65	13.5	44.4
NGC 0169	$00^h36^m51\overset{s}{.}7$	23°59′25.″3	72	87*	0.01525	15	5.0	10.1	−31.0	98	19.4	45.4
NGC 0171	$00^h37^m21\overset{s}{.}5$	19°56′03.″3	33	101*	0.01277	14	4.9	8.0	−47.0	57	15.8	61.3
NGC 0180	$00^h37^m57\overset{s}{.}7$	08°38′06.″7	45	163*	0.01743	13	5.6	8.9	−30.0	61	20.2	65.6
NGC 0693	$01^h50^m30\overset{s}{.}8$	06°08′42.″8	90	106*	0.00498	17	5.1	8.9	−43.0	17	11.6	62.7
NGC 0731	$01^h54^m56\overset{s}{.}2$	09°00′38.″9	20	155*	0.01296	12	5.1	8.2	−49.0	55	10.4	50.9
NGC 0768	$01^h58^m40\overset{s}{.}9$	00°31′45.″2	68	28*	0.02308	13	5.3	8.3	−46.0	80	15.6	46.5
NGC 0955	$02^h30^m33\overset{s}{.}1$	01°06′30.″3	90	19*	0.00489	17	5.2	8.5	−44.0	24	9.4	80.7
NGC 1056	$02^h42^m48\overset{s}{.}3$	28°34′26.″8	53	162*	0.00528	15	4.8	10.9	−27.0	30	7.9	55.9
NGC 1542	$04^h17^m14\overset{s}{.}1$	04°46′53.″9	90	127*	0.01235	18	4.8	8.2	−42.0	70	9.5	36.9
NGC 2449	$07^h47^m20\overset{s}{.}2$	26°55′49.″1	70	135*	0.01652	15	6.0	7.6	−76.0	43	12.8	43.4
NGC 2540	$08^h12^m46\overset{s}{.}4$	26°21′42.″6	55	123*	0.02088	17	5.7	9.7	−21.0	75	15.4	37.2
NGC 2554	$08^h17^m53\overset{s}{.}5$	23°28′19.″9	47	153*	0.01365	18	5.9	8.3	−61.0	60	17.5	61.3
NGC 2595	$08^h27^m41\overset{s}{.}9$	21°28′44.″7	35	30*	0.01429	18	5.8	8.5	−63.0	64	24.1	49.8
NGC 2596	$08^h27^m26\overset{s}{.}4$	17°17′02.″3	68	63*	0.01964	17	5.3	8.5	−32.0	82	11.7	41.4
NGC 3300	$10^h36^m38\overset{s}{.}4$	14°10′16.″1	57	173*	0.01012	16	5.8	7.7	−76.0	47	13.3	45.4
NGC 6427	$17^h43^m38\overset{s}{.}5$	25°29′38.″1	70	35*	0.01088	15	4.9	10.3	−29.0	45	8.9	46.5
NGC 7025	$21^h07^m47\overset{s}{.}3$	16°20′09.″1	54	44*	0.01639	13	4.9	9.1	−49.0	75	18.2	59.9
NGC 7194	$22^h03^m30\overset{s}{.}9$	12°38′12.″4	43	17*	0.02713	13	5.6	9.5	−30.0	123	11.9	39.5
NGC 7311	$22^h34^m06\overset{s}{.}7$	05°34′11.″6	62	11*	0.01495	13	5.1	8.9	−41.0	61	10.6	44.4
NGC 7321	$22^h36^m28\overset{s}{.}0$	21°37′18.″5	56	17*	0.02372	14	4.9	9.7	−30.0	104	12.0	42.4
NGC 7364	$22^h44^m24\overset{s}{.}3$	00°09′43.″5	54	66*	0.01605	14	4.5	8.4	86.0	68	10.6	49.8
NGC 7466	$23^h02^m03\overset{s}{.}4$	27°03′10.″1	66	25*	0.02483	13	5.2	11.6	−19.0	92	12.6	46.5
NGC 7489	$23^h07^m32\overset{s}{.}6$	22°59′53.″6	63	165*	0.02071	14	5.0	9.7	−30.0	70	16.6	36.9
NGC 7625	$23^h20^m30\overset{s}{.}0$	17°13′35.″0	40	45*	0.00557	15	5.3	7.9	−53.0	24	9.8	44.4
NGC 7716	$23^h36^m31\overset{s}{.}4$	00°17′50.″2	44	34*	0.00851	15	4.9	7.5	−69.0	36	14.2	54.6
UGC 00312	$00^h31^m23\overset{s}{.}9$	08°28′00.″6	63	7*	0.01424	15	5.4	7.9	−57.0	57	13.3	44.4
UGC 00335 NED 02	$00^h33^m57\overset{s}{.}3$	07°16′05.″9	50	147*	0.01812	13	5.4	9.0	−31.0	78	16.6	44.4
UGC 01123	$01^h34^m07\overset{s}{.}9$	01°01′56.″2	75	70*	0.01615	12	5.2	8.4	−43.0	54	9.8	36.9
UGC 01368	$01^h54^m13\overset{s}{.}1$	07°53′01.″1	73	51*	0.02653	12	5.5	7.0	−70.0	108	10.9	40.5
UGC 01938	$02^h28^m22\overset{s}{.}1$	23°12′52.″7	78	155*	0.02108	14	5.2	9.4	−25.0	96	8.6	35.2
UGC 02099	$02^h37^m13\overset{s}{.}0$	21°34′04.″0	66	138*	0.02737	14	5.4	10.4	−31.0	118	13.7	35.2
UGC 04240	$08^h08^m06\overset{s}{.}1$	14°50′16.″3	76	178*	0.02886	12	5.3	8.3	87.0	163	10.2	37.8
UGC 04245	$08^h08^m45\overset{s}{.}7$	18°11′39.″0	70	107*	0.01733	17	5.0	9.0	−32.0	75	14.5	42.4
UGC 04455	$08^h31^m32\overset{s}{.}8$	01°11′51.″8	47	13*	0.03044	16	5.0	7.7	−81.0	128	7.9	25.0
UGC 05396	$10^h01^m40\overset{s}{.}4$	10°45′23.″0	75	145*	0.01798	13	5.7	7.7	−87.0	76	13.9	44.4
UGC 08322	$13^h15^m00\overset{s}{.}9$	12°43′31.″0	73	36*	0.02540	15	5.8	7.9	−82.0	98	8.5	33.7
UGC 08781	$13^h52^m22\overset{s}{.}7$	21°32′22.″0	50	161*	0.02513	15	6.3	7.9	−61.0	115	12.0	47.5
UGC 10972	$17^h46^m21\overset{s}{.}8$	26°32′36.″9	78	55*	0.01539	15	4.8	10.7	−28.0	63	19.0	62.7
UGC 11649	$20^h55^m27\overset{s}{.}6$	01°13′30.″9	42	90*	0.01252	14	5.3	8.4	−42.0	60	14.5	43.4
UGC 11680 NED 02	$21^h07^m45\overset{s}{.}8$	03°52′40.″4	40	205*	0.02615	12	4.7	8.3	89.0	111	9.9	20.8
UGC 11717	$21^h18^m35\overset{s}{.}4$	19°43′07.″0	60	39*	0.02088	19	5.5	8.6	−54.0	90	11.8	36.1
UGC 11792	$21^h42^m12\overset{s}{.}7$	05°36′55.″1	78	160*	0.01586	18	5.1	8.2	87.0	68	17.4	40.5
UGC 11958	$22^h14^m46\overset{s}{.}8$	13°50′27.″2	50	143*	0.02618	13	5.5	9.8	−31.0	112	17.0	59.9
UGC 11982	$22^h18^m52\overset{s}{.}9$	01°03′31.″2	78	171*	0.01554	14	4.5	8.3	−87.0	69	12.3	36.9
UGC 12224	$22^h52^m38\overset{s}{.}3$	06°05′37.″2	45	46*	0.01156	13	5.2	8.9	−41.0	50	22.4	44.4
UGC 12250	$22^h55^m35\overset{s}{.}8$	12°47′24.″9	53	12*	0.02405	12	5.4	9.4	−36.0	92	12.8	49.8
UGC 12274	$22^h58^m19\overset{s}{.}5$	26°03′43.″3	73	142*	0.02538	13	5.0	11.4	−23.0	110	12.4	40.5
UGC 12348	$23^h05^m18\overset{s}{.}8$	00°11′22.″3	75	136*	0.02510	13	5.1	7.1	−74.0	108	12.4	38.6
VV 488 NED 02	$22^h56^m50\overset{s}{.}8$	08°58′03.″1	82	73*	0.01632	16	4.1	8.8	−86.0	70	13.3	62.7

Note. Column (1): galaxy name. Column (2): R.A. (J2000) of the galaxy optical center. Column (3): decl. (J2000) of the galaxy optical center. Column (4): optical SDSS r-band inclination. Column (5): optical SDSS r-band PA, calculated east of north. If no asterisk is given, we give the receding side of the galaxy. Column (6): stellar redshift. Column (7): rms flux in 10 km s^{-1} channels. Column (8): minor axis of the synthesized beam. Column (9): major axis of the synthesized beam. Column (10): PA of the synthesized beam. Column (11): distance. Column (12): effective radius. Column (13): optical size of the major axis measured at 25 mag arcsec^{-2} in the B band. Columns (2) and (3) are drawn from NED. Column (4) is derived by finding the best fit for the SDSS z-band contours at $r \sim r_{25}$ as described in Section 3.1. Columns (5) and (6) are drawn from HyperLEDA, except when kinematic information overruled. Column (11) is derived from column (6) assuming a ΛCDM cosmology with $\Omega_\Lambda = 0.7$, $\Omega_{DM} = 0.3$, and $H_0 = 69.7$ km s^{-1} Mpc^{-1}. Column (12) is taken from CALIFA. Column (13) is taken from de Vaucouleurs et al. (1991).

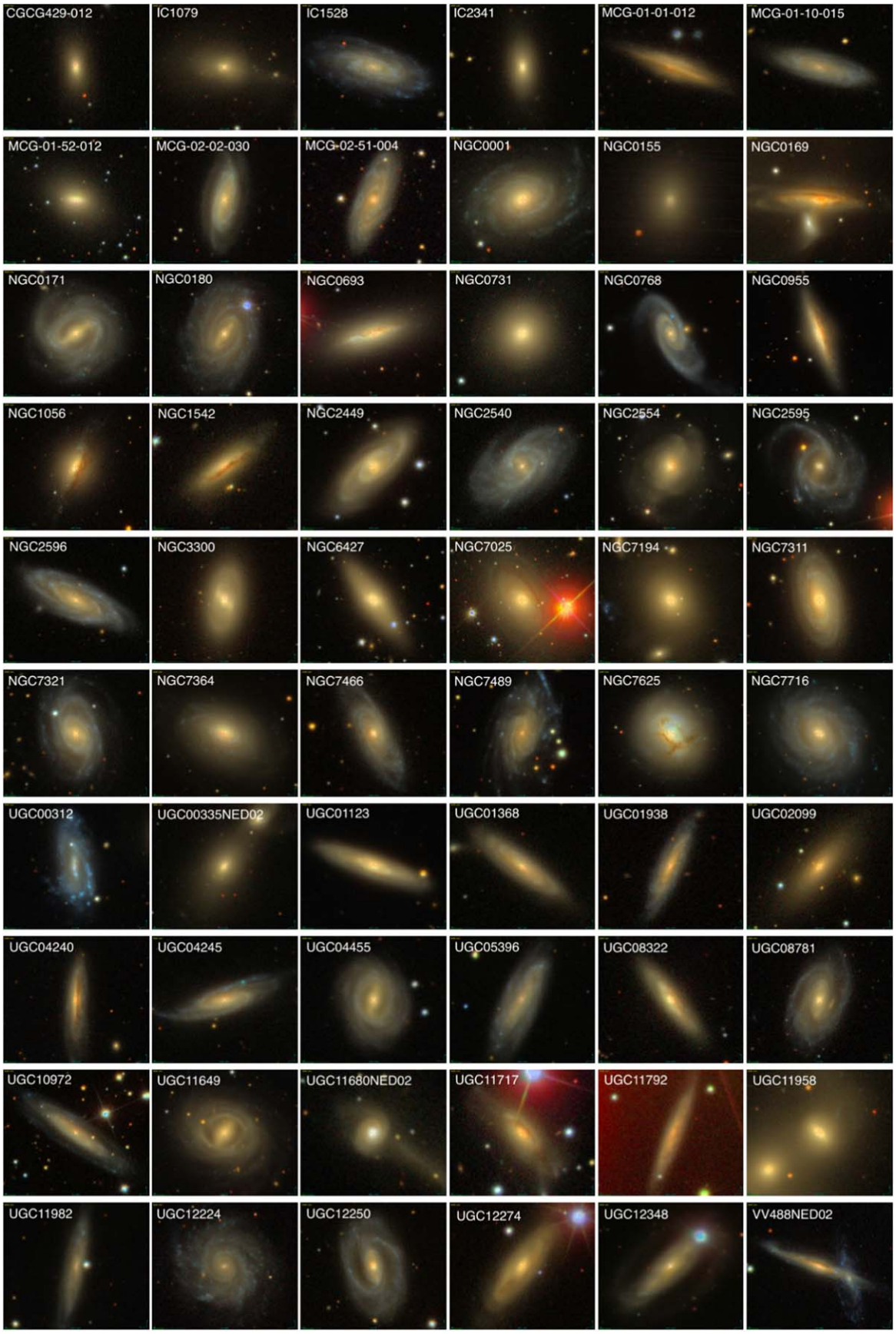

Figure 2. SDSS *r*- (red channel), *i*- (green channel), and *z*-band (blue channel) composite images for the 60 galaxies encompassed by the ACA EDGE survey. These local galaxies show a broad variety of morphologies representative of the distribution of galaxies in the local Universe. This enables one of the main ACA EDGE goals, to analyze the star formation quenching mechanisms at different evolutionary stages.

1. *Hα mask (33 galaxies)*. We construct a mask using the central Hα velocity map from CALIFA and including around it a velocity region [−FWHM, +FWHM] following the FWHM prescription from Figure 2 in Villanueva et al. (2021). Hα spaxels with S/N < 5 in intensity are excluded from the mask. This approach assumes that the kinematics of the CO are similar to the kinematics of the Hα (e.g., Levy et al. 2018).
2. *Rotation mask (25 galaxies)*. We construct a mask assuming a very simple generic rotation curve that assumes the velocity is constant for $r > 5''$ and increases linearly inside this radius. We adopt the maximum apparent rotation velocity reported in H I by HyperLEDA (`vmaxg` calculated from the 21 cm line, which we call $V_{\rm HI,max}$ here; Bottinelli et al. 1982, 1990) and adopt the systemic stellar velocity from CALIFA. We include the same velocity region around this central velocity as for the previous mask. This mask only extends to $r = r_{25}$. The direction of rotation is decided based on the Hα or CO velocity field (if available) or, ultimately, if neither are detected, based on comparing the flux recovered between the two senses of rotation. This approach assumes that the galaxy is predominantly rotating and that the CO emission spans the same velocities as the H I.
3. *Flat mask (2 galaxies)*. We construct a mask centered at the stellar systemic velocity, including all the channels inside the maximum apparent rotation velocity reported by HyperLEDA and extending out to $r = 0.5r_{25}$. This approach does not assume any particular kinematics and is the most relaxed of the three, although it will also include more noise.

Our final step is to combine (through a logical `OR` operation) the best mask derived from this procedure with the dilated mask obtained from the CO in order to obtain the final mask.

We generate moment 0 maps (integrated intensity of the spectrum along the spectral axis) from the CO(2−1) spectral line cubes in units of Jy beam^{-1} km s^{-1} and after multiplying them by our mask (see Figure 3). To obtain the uncertainties of the moment 0 maps, we compute the rms in the signal-free part of the spectrum in each spaxel, $\sigma_{\rm i}$, and use the equation

$$u_{\rm i} = \sigma_{\rm i}\sqrt{N}\Delta v. \quad (1)$$

Here, N is the number of channels included by the mask, and Δv is the channel width (in km s^{-1}). We also compute the velocity (moment 1) and peak S/N (S/N$_{\rm peak}$) maps.

The moment 1 maps (or CO velocity maps, in units of km s^{-1}) are derived by multiplying the CO data cubes by the mask and using

$$M_{1,\rm i} = \frac{\Sigma I_{\rm i,j} v_{\rm j}}{M_{0,\rm i}}, \quad (2)$$

where $I_{\rm i,j}$ is the CO intensity in the jth spectral channel of the ith spaxel, $v_{\rm j}$ is the velocity of the jth channel, and M_0 is the moment 0 map. Finally, we blank the pixels outside the 2σ contour for M_0. We also computed maps of the peak S/N, S/N$_{\rm peak,i}$, at each position. We use the following equation:

$$\mathrm{S/N}_{\rm peak} = \frac{\max(I_{\rm i,j})}{\sigma_{\rm i}}, \quad (3)$$

where $\max(I_{\rm i,j})$ is the maximum value of the CO intensity within the spectrum of the ith spaxel. Both velocity and S/N$_{\rm peak}$ maps are included in Figure 3.

We compare the ^{12}CO(2−1) integrated fluxes for ACA EDGE galaxies to those from Colombo et al. (2020), who report ^{12}CO(2−1) fluxes for 51 of our galaxies using APEX observations at 26.″3 resolution and 30 km s^{-1} channel width (as part of the APEX EDGE survey). The APEX EDGE survey arises from either the necessity of exploring whether star formation quenching is driven by the reduction in molecular gas content, a change in the star formation efficiency (SFE) of the molecular gas, or both. To address this, Colombo et al. (2020) use the ^{12}CO(1–0) maps from the EDGE survey included in Bolatto et al. (2017) in combination with APEX ^{12}CO(2−1) measurements. With these maps, they investigate the center of more than 470 galaxies selected from the CALIFA survey (Sánchez et al. 2012) at different quenching stages. To compare the fluxes, we convolve our CO data cubes to match the APEX angular resolution, and we take the spectrum of the pixel located at the galaxy center (see Figure 4), correcting by the recommended APEX main beam antenna efficiency (for the PI230 receiver at this frequency, $\eta_{\rm mb} = 0.80$). Finally, we integrate the spectra over a spectral window defined by visual inspection (typically ∼500 km s^{-1} wide). Uncertainties are computed by deriving the rms from the signal-free part of the spectrum and using Equation (1). For nondetections, we estimate 1σ upper limits by computing the rms over the velocity window given by $V_{\rm H\,I,max}$ and using Equation (1). Discrepancies between both measurements can, in principle, be attributed to inconsistencies in calibration, flux that is resolved out or lost due to imperfect deconvolution for ACA measurements, or pointing for APEX. Although there are some discrepancies between the two data sets and a handful of cases with incomplete ACA spectral coverage, Figure 5 shows that there is reasonable consistency between the ACA and APEX integrated CO fluxes. On average, we find that the median ACA-to-APEX flux ratio is 0.82.

2.4. The CALIFA Survey and Ancillary Data

The CALIFA survey (Sánchez et al. 2012) comprises a sample of over 800 galaxies at $z \approx 0$. The data were acquired using the PMAS/PPAK IFU instrument (Roth et al. 2005) at the 3.5 m telescope of the Calar Alto Observatory. PMAS/PPAK uses 331 fibers each with a diameter of 2.″7 in an hexagonal shape covering an FoV of 1 arcmin^2. Its average spectral resolution is $\lambda/\Delta\lambda \sim 850$ at ∼5000 Å for a wavelength range that spans from $\lambda = 3745$ to 7300 Å. As mentioned in Section 2.1, CALIFA galaxies are angular size–selected such that their isophotal diameters, D_{25}, match well with the PMAS/PPAK FoV. They range from 45″ to 80″ in the SDSS r band (Walcher et al. 2014). The CALIFA survey uses a data reduction pipeline designed to produce data cubes with more than 5000 spectra with a sampling of $1'' \times 1''$. For more details, see Sánchez et al. (2016a). These cubes are processed using `PIPE3D` (Sánchez et al. 2016b, 2016c) to generate maps of derived quantities.

The final data compilation also contains ancillary data, including information from HyperLEDA and the NASA/IPAC Extragalactic Database (NED[15]), among others.

[15] https://ned.ipac.caltech.edu/

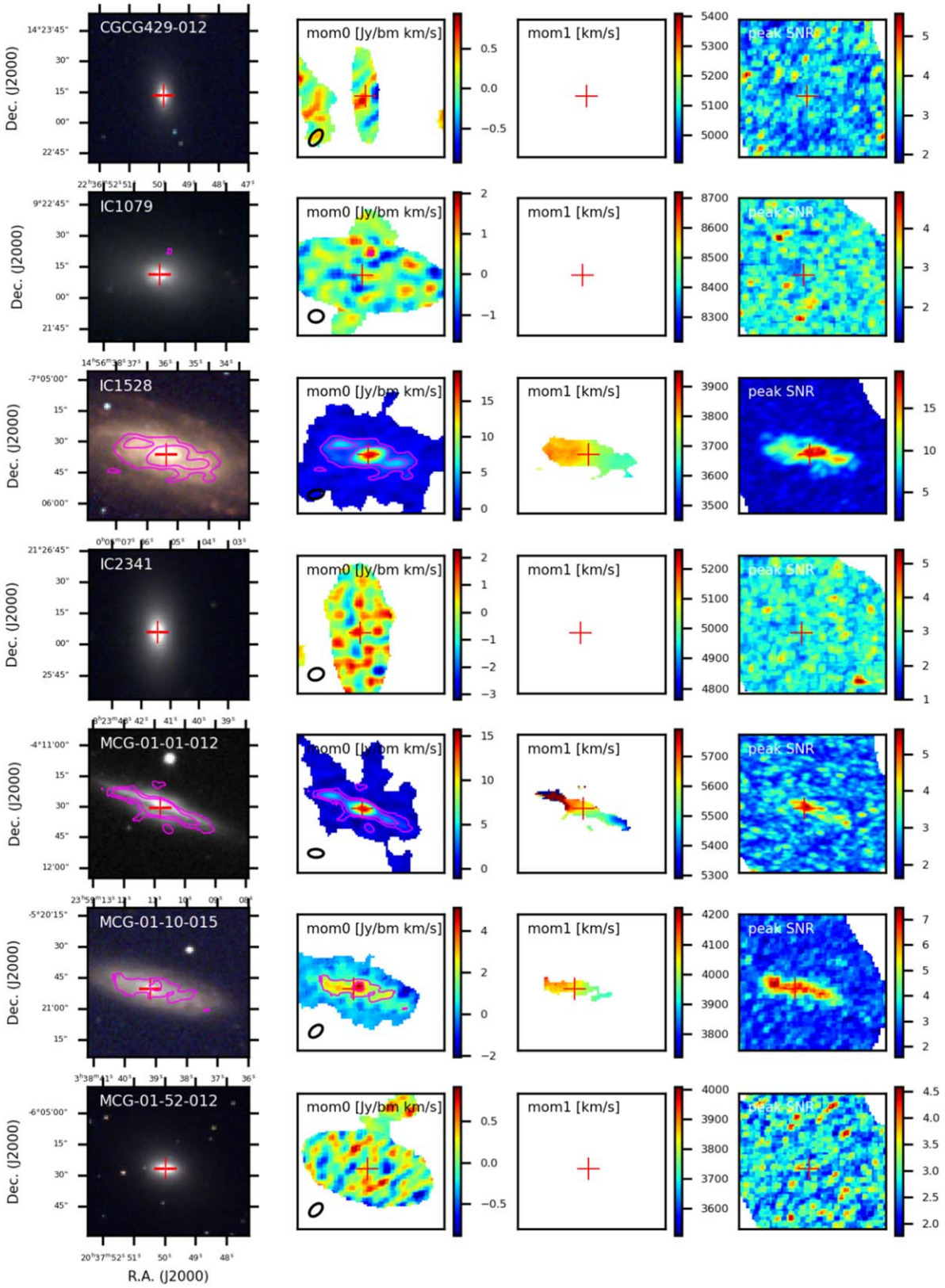

Figure 3. ACA EDGE data products for each galaxy. Panels cover an area of $1\farcm25 \times 1\farcm25$. The first column shows the SDSS *riz* multicolor image with contours from our integrated intensity masked map overlaid. Contours correspond to 2σ and 5σ CO(2−1) emission line levels. From left to right, the following columns show the CO(2−1) emission line intensity (moment 0, in units of Jy beam^{-1} km s^{-1}), velocity (moment 1, in units of km s^{-1}), and S/N peak maps, respectively. The red plus signs are the optical centers (columns (2) and (3) of Table 1). The black ellipses in the bottom left corner are the beam size of the CO(2−1) data. Panels for the remainder of the survey can be found in the Appendix.

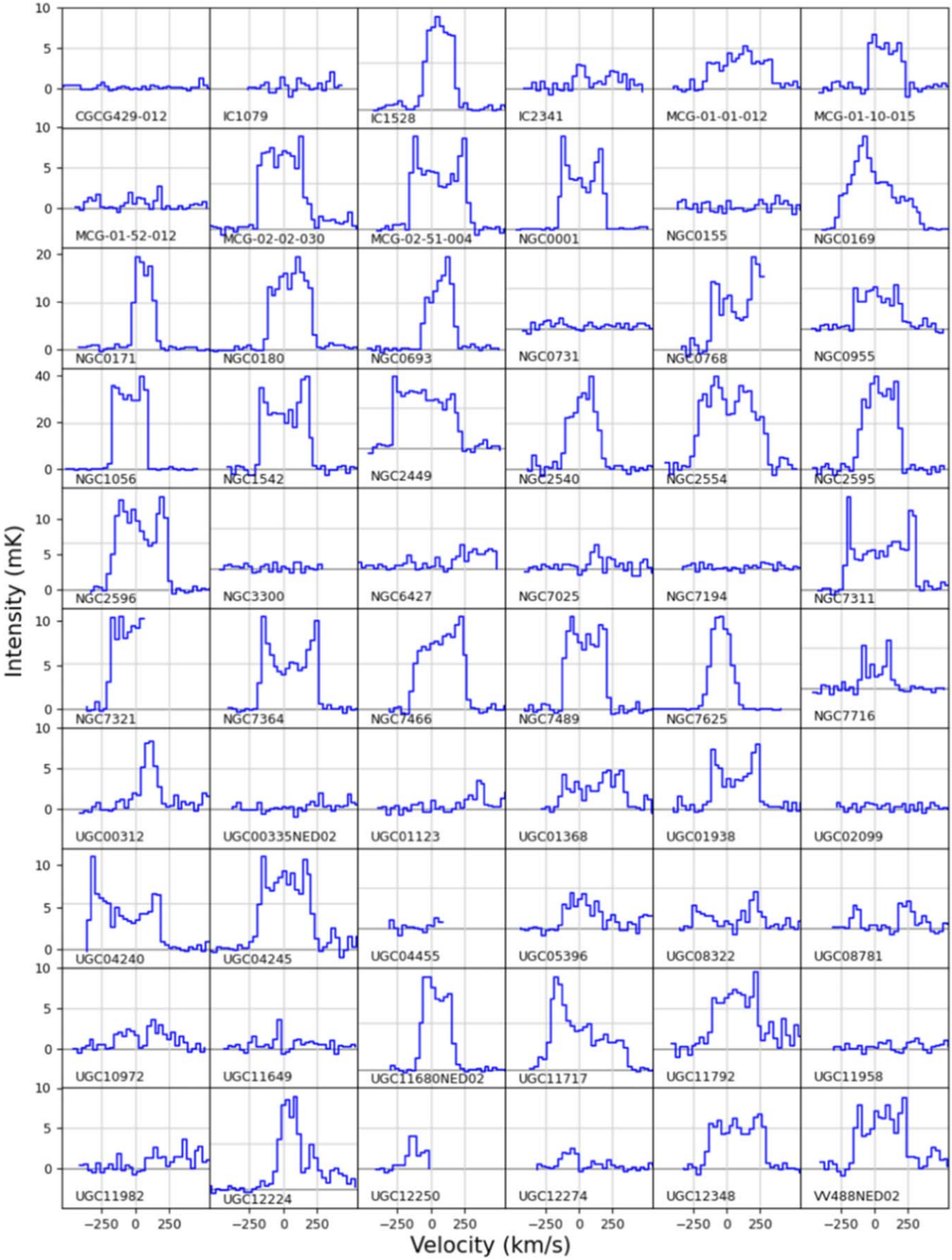

Figure 4. CO(2−1) spectra for ACA data cubes convolved to 1.″1 and 30 km s^{-1} channel width for the 60 galaxies. The spectra are taken from the central pixel located at the optical center (columns (2) and (3) in Table 1), and velocities are centered on the stellar redshift.

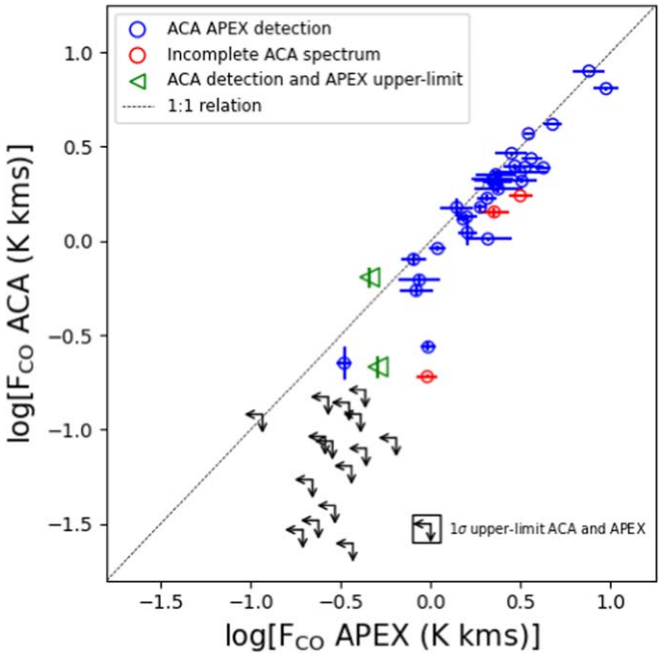

Figure 5. Comparison of the integrated CO($J = 2-1$) emission line flux between the ACA (this work) and APEX (Colombo et al. 2020) data sets for 51 ACA galaxies. ACA fluxes are derived after convolving the data cubes to match the APEX angular resolution (26.″3). The red dots correspond to NGC 0768, NGC 7321, and UGC 12250, which have incomplete ACA spectral coverage (see Figure 4). The green arrows are UGC 08322 and UGC 12274, which are detected by ACA but not APEX (see Table 2). The figure shows good agreement between the ACA and APEX fluxes. However, fluxes measured by APEX are, on average, ∼20% brighter than in ACA, likely due to calibration differences. Note that a lack of a detection by ACA in a 26″ beam does not imply the source is not detected by ACA; for interferometric data, convolution results in removing visibilities in long baselines (and thus collecting area and sensitivity).

3. Methods and Products

3.1. Basic Equations and Assumptions

To compute the extinction-corrected SFRs, we estimate the extinction (based on the Balmer decrement; see Bolatto et al. 2017) for each 1″ spaxel using the equation

$$A_{\mathrm{H}\alpha} = 5.86 \log\left(\frac{F_{\mathrm{H}\alpha}}{2.86 F_{\mathrm{H}\beta}}\right), \quad (4)$$

where $F_{\mathrm{H}\alpha}$ and $F_{\mathrm{H}\beta}$ are the fluxes of the respective Balmer lines, and the coefficients assume a Cardelli et al. (1989) extinction curve and an unextinguished flux ratio of 2.86 for case B recombination. Then, the corresponding SFR (in $M_\odot\,\mathrm{yr}^{-1}$) is obtained using (Rosa-González et al. 2002)

$$\mathrm{SFR} = 1.6 \times 7.9 \times 10^{-42} F_{\mathrm{H}\alpha} 10^{\frac{A_{\mathrm{H}\alpha}}{2.5}}, \quad (5)$$

which includes a correction factor of 1.6 to move from a Salpeter initial mass function (IMF; as adopted by PIPE3D) to the more commonly used Kroupa IMF (Speagle et al. 2014). We do this to compare our results with those for other galaxy surveys. We use this to compute the SFR surface density, Σ_{SFR} in $M_\odot\ \mathrm{yr}^{-1}\,\mathrm{kpc}^{-2}$, by dividing by the face-on area corresponding to a 1″ spaxel, given the angular diameter distance to the galaxy. In order to produce smooth SFR maps, we process the Hα and Hβ fluxes by applying the following recipe.

1. We select pixels with non-NaN values for $F_{\mathrm{H}\alpha}$.
2. We adopt a minimum Hα-to-Hβ flux ratio, $F_{\mathrm{H}\alpha}/F_{\mathrm{H}\beta}$, of 2.86. Therefore, if $F_{\mathrm{H}\alpha}/F_{\mathrm{H}\beta} < 2.86$, we impose $F_{\mathrm{H}\alpha}/F_{\mathrm{H}\beta} = 2.86$ (so $A_{\mathrm{H}\alpha} = 0$).
3. If $F_{\mathrm{H}\beta}$ is a NaN value for a given pixel, then we take the average value of $A_{\mathrm{H}\alpha}$ (for pixels with $A_{\mathrm{H}\alpha} > 0.0$) of the whole $A_{\mathrm{H}\alpha}$ map.

We obtain the stellar mass surface density, $\Sigma_\star$, from the stellar maps derived by PIPE3D. We correct the maps from the spatial binning effect by applying the dezonification correction provided by PIPE3D data cubes. This is to weight the $\Sigma_\star$ maps by the relative contribution to flux in the V band for each spaxel to the flux intensity of the bin in which it is aggregated (for more details, see Sánchez et al. 2016c). Finally, we mask the $\Sigma_\star$ maps to avoid the flux contribution from field stars, and we include the 1.6 correction factor to move from a Salpeter to a Kroupa IMF.

The molecular gas surface density, Σ_{mol}, is derived from the integrated CO intensity, $I_{\mathrm{CO}(2-1)}$, by adopting a constant CO-to-H_2 conversion factor that is based on observations of the Milky Way: $X_{\mathrm{CO}} = 2 \times 10^{20}\ \mathrm{cm}^{-2}\ (\mathrm{K\,km\,s}^{-1})^{-1}$, or, equivalently, $\alpha_{\mathrm{CO,MW}} = 4.3\ M_\odot\ (\mathrm{K\ km\ s}^{-1}\ \mathrm{pc}^2)^{-1}$ for the CO($J = 1$–0) line (Walter et al. 2008). We also test how our results depend on our adopted prescription by using the CO-to-H_2 conversion factor from Equation (31) in Bolatto et al. (2013),

$$\alpha_{\mathrm{CO}}(Z', \Sigma_{\mathrm{total}}) = 2.9 \exp\left(\frac{+0.4}{Z' \Sigma^{100}_{\mathrm{GMC}}}\right)\left(\frac{\Sigma_{\mathrm{total}}}{100\ M_\odot\ \mathrm{pc}^2}\right)^{-\gamma}, \quad (6)$$

in $M_\odot\ (\mathrm{K\ km\ s}^{-1}\,\mathrm{pc}^{-2})^{-1}$. $\gamma \approx 0.5$ for $\Sigma_{\mathrm{total}} > 100\ M_\odot\ \mathrm{pc}^{-2}$, and $\gamma = 0$ otherwise. Additionally, the metallicity is normalized to the solar one, $Z' = [\mathrm{O/H}]/[\mathrm{O/H}]_\odot$, where $[\mathrm{O/H}]_\odot = 4.9 \times 10^{-4}$ (Baumgartner & Mushotzky 2006), $\Sigma^{100}_{\mathrm{GMC}}$ is the average surface density of molecular gas in units of $100\,M_\odot\,\mathrm{pc}^{-2}$, and Σ_{total} is the combined gas plus stellar surface density on kiloparsec scales. We are also interested in the global variations of $\alpha_{\mathrm{CO}}(Z', \Sigma_{\mathrm{total}})$. To do so, we adopt $\Sigma^{100}_{\mathrm{GMC}} = 1$ and derive Z' using the metallicity–stellar mass relation (based on the O3N2 calibrator; Marino et al. 2013) for CALIFA galaxies from Sánchez et al. (2017). We use the following expression to obtain Σ_{mol}:

$$\Sigma_{\mathrm{mol}} = \frac{\alpha_{\mathrm{CO}}}{R_{21}} \cos(i) I_{\mathrm{CO}(2-1)}, \quad (7)$$

which adopts the average line luminosity ratio of $R_{21} = I_{\mathrm{CO}(2-1)}/I_{\mathrm{CO}(1-0)} = 0.65$ based on Leroy et al. (2013) and den Brok et al. (2021), measured at kiloparsec scales; i is the inclination of the galaxy. This equation takes into account the mass correction due to the cosmic abundance of helium. Although i is generally drawn from HyperLEDA, we use SDSS z-band images to obtain a better constraint on the inclination (particularly for galaxies with $i > 60°$). To do so, we fit an ellipse to the SDSS z-band contour for a major axis $A_{\mathrm{maj}} \sim 1.2 r_{25}$. We obtain the ratio between the minor and major axes, $A_{\mathrm{min}}/A_{\mathrm{maj}}$, and compute the inclination by taking $i = \arccos[A_{\mathrm{min}}/A_{\mathrm{maj}}]$ (see column (4) in Table 1). This assumes an infinitely thin disk and introduces errors for $i > 85°$, but we discard highly inclined galaxies from our analysis anyway, since most derived quantities are highly uncertain.

To compute the global values of the molecular gas mass, $M_{\rm mol}$, $M_\star$, and SFR (Q_i quantities), we use the following equation:

$$Q_{\rm i} = \int_A \Sigma_{\rm i}(r) dA, \tag{8}$$

where A is the area within a circle defined by the geometrical parameters included in Table 1 (with radius r_{25} and centered at the optical center), $\Sigma_{\rm i}$ is the surface densities for the pixels within A, and i = SFR, mol, or $\star$.

We integrate the surface densities for the molecular gas, stars (assuming that they are distributed along a thin disk), and SFR to obtain the stellar mass, molecular gas mass, and SFR within the bulge:

$$M_{{\rm b},i} = 2\pi \int_0^{R_{\rm b}} \Sigma_i(r)\, r dr, \tag{9}$$

where $R_{\rm b}$ is the bulge radius for the stellar component (see Section 3.3 for more details), and i = mol, $\star$, or SFR. We then calculate the integrated ratios as the ratio of the integrated masses and the SFR.

Finally, we compute the resolved $\rm SFE_{mol}$ (in units of $\rm yr^{-1}$) for each pixel,

$$\rm SFE_{mol} = \frac{\Sigma_{SFR}}{\Sigma_{mol}}. \tag{10}$$

In a similar way, we calculate the resolved molecular-to-stellar mass fraction, $rR_\star^{\rm mol} = \Sigma_{\rm mol}/\Sigma_\star$, and the specific SFR, $\rm sSFR = \Sigma_{SFR}/\Sigma_\star$ (in units of $\rm yr^{-1}$).

3.2. Radial Profiles

We obtain stellar and molecular gas radial profiles for a subsample of 30 galaxies with inclinations of $\leqslant 70°$ and 5σ integrated CO detections (see Section 4.1), which represent well the distributions of stellar masses and morphologies of the full ACA EDGE sample (see Table 2). We also select spaxels with 3σ CO detections. We derive these profiles by measuring the average azimuthal CO, stellar, and SFR surface densities in elliptical annuli in the CO(2−1) data cubes. Figure 6 shows the molecular gas radial profiles (blue solid line) and their $\pm 1\sigma$ uncertainties (blue shaded areas), which are corrected by inclination (i.e., multiplied by a factor of cos(i)). Annuli are centered on the optical galaxy position and aligned with the centered major-axis PA (column (5) in Table 1). We compute the average $I_{\rm CO(2-1)}$ for a given annulus by summing the velocity-integrated CO line emission intensities from the total pixels within an annulus $\sim 5''$ wide (average of the minor beam axes), and then we use Equation (7) (adopting the constant $\alpha_{\rm CO}$ prescription; see Section 3.1) to obtain the molecular gas surface density, $\Sigma_{\rm mol}$.

We implement the same method (averaging over all pixels in an annulus) for the SFR and stars. Stellar and SFR radial profiles are shown in Figure 6 by the red solid and brown dotted lines, respectively. We remove SFRs at $r < 0.5R_{\rm e}$ for galaxies classified as LINER or AGN (bottom left corners in Figure 6) since Hα in this region is susceptible to LINER/AGN contamination (see Section 4.2.2 for more details).

3.3. Bulge Radii and Masses

In order to test the star formation quenching mechanisms within the bulge region (see Section 4.2.2), we derive the radius of the bulge, $R_{\rm b}$, for the 30 ACA EDGE galaxies included in Figure 6. We characterize the bulge-dominated region by identifying the galactocentric radius where there is a break with respect to the stellar radial profiles. Similar to Villanueva et al. (2022), we adopt $R_{\rm b} = 1$ kpc for spiral galaxies where we do not identify a clear break or they have a predominant bar (e.g., SB galaxies have stellar radial profiles mostly dominated by bars and stellar disks rather than bulges). Since previous studies have shown that bulges for spirals are typically $\lesssim$1.5 kpc (e.g., Regan et al. 2001; Méndez-Abreu et al. 2017; Villanueva et al. 2021), we use the stellar and SFR maps at CALIFA's native resolution of $2\farcs7$ to obtain the best physical resolution available ($\sim$0.9 kpc at the median distance of ACA EDGE galaxies). Bulge radius distributions for main-sequence and green valley galaxies are centered at $\log[R_{\rm b}/({\rm kpc})] \sim 0.15$ and ~ -0.1, which are slightly larger than those found by Querejeta et al. (2021), who compute the radius for the central regions (including small bulges and nuclei) of 74 nearby galaxies selected from PHANGS. By implementing a photometric decomposition using GALFIT (Peng et al. 2010), they obtain a mean value of $\log[R_{\rm center}/r_{25}] \sim -1.5$, which, on average, is lower than that of our main-sequence galaxies ($\log[R_{\rm center}/r_{25}] \sim -1.0$). While ACA EDGE attempts to reflect the broad range of galaxy morphologies in the local Universe, PHANGS emphasizes late-type spirals of somewhat lower mass ($9.25 \leqslant \log[M_\star/M_\odot] \leqslant 11.25$), which could result in shorter bulge radii. Finally, red cloud galaxies have the largest bulge radii, with $R_{\rm b}$ distributions centered at $\log[R_{\rm B}/({\rm kpc})] \sim 0.35$. These results are consistent with observational evidence. For instance, Mendel et al. (2013) present a catalog of bulge, disk, and total stellar mass estimates for $\sim$660,000 galaxies from SDSS DR7 based on g- and r-band photometry published in Simard et al. (2011) and using GIM2D (Simard et al. 2002). By fitting Sérsic profiles ($n_{\rm S}$; Sersic 1968) to elliptical, disk, and bulge+disk, they find a Sérsic index distribution centered at larger values for the former ($n_{\rm S} \sim 5$) when compared to the latter two groups ($n_{\rm S} \sim 1$). In addition, Méndez-Abreu et al. (2017) implement a two-dimensional photometric decomposition using GASP2D (Méndez-Abreu et al. 2008, 2014) for 404 CALIFA galaxies using g, r, and i SDSS images, including 28 ACA EDGE galaxies in their analysis. We obtain a close 1:1 relation when comparing the two sets of bulge radii (OLS $R_{\rm b,CALIFA} = [0.83 \pm 0.10] \times R_{\rm b,ACA\ EDGE}$), which also show a strong correlation between them (Pearson $r_{\rm p} = 0.92$; p-value $< < 0.01$).

Using $R_{\rm b}$, we compute the bulge mass, $M_{\rm b}$, in terms of the total stellar mass after numerically integrating the stellar profiles using Equation (9). Table 2 summarizes the properties of the 60 ACA EDGE galaxies, together with the values of $R_{\rm b}$ and $M_{\rm b}$ (columns (10) and (11)). Columns (4), (8), and (9) list $M_{\rm mol}$, $l_\star$, and $l_{\rm mol}$, respectively; the latter two are calculated from radial profiles in Section 4.1.2.

4. Results and Discussion

In the next subsections, we present the main properties of the 60 galaxies included in the ACA EDGE survey. To do so, we divide our results into global (i.e., quantities derived from integrated measurements) and spatially resolved (i.e., quantities derived from pixel measurements). Unless otherwise mentioned, we estimate the molecular gas-related quantities by adopting a constant Milky Way CO-to-H_2 conversion factor (see Section 3.1).

Table 2
Main Properties of the ACA EDGE Galaxies

Name	$\log[M_\star]$ ($M_\odot$)	log[SFR] ($M_\odot$ yr^{-1})	$\log[M_{\rm mol}]$ ($M_\odot$)	Morph. Class	Nuclear	ΔSFR Class	Quenching Stage	$l_\star$ (kpc)	$l_{\rm CO}$ (kpc)	$R_{\rm b}$ (kpc)	$M_{\rm b}$ ($M_\odot/M_\star$)
(1)	(2)	(3)	(4)	(5)	(6)	(7)	(8)	(9)	(10)	(11)	(12)
CGCG 429-012	10.46	−1.68	<6.77	E0	⋯	RS	fR	⋯	⋯	⋯	⋯
IC 1079	11.2	−1.23	8.86 ± 0.17	E	⋯	RS	nR	9.12 ± 0.98	⋯	10.99 ± 1.07	0.14 ± 0.19
IC 1528	10.76	0.23	8.83 ± 0.02	SBb	⋯	MS	SF	4.8 ± 2.01	5.13 ± 1.25	0.52 ± 0.39	0.01 ± 0.38
IC 2341	10.86	−0.8	<7.4	S0-	⋯	RS	fR	⋯	⋯	⋯	⋯
MCG-01-01-012	11.19	0.21	7.58 ± 0.02	SAab	⋯	GV	MX	⋯	⋯	⋯	⋯
MCG-01-10-015	9.95	−0.01	8.32 ± 0.03	Sd	⋯	MS	SF	⋯	⋯	⋯	⋯
MCG-01-52-012	10.37	−0.79	<6.56	S0-	⋯	GV	nR	⋯	⋯	⋯	⋯
MCG-02-02-030	10.81	0.03	8.52 ± 0.02	SBa	AGN	MS	QnR	3.95 ± 1.43	23.27 ± 49.75	1.35 ± 0.28	0.1 ± 0.07
MCG-02-51-004	10.94	0.64	9.19 ± 0.02	Sd	⋯	MS	SF	6.93 ± 0.74	19.56 ± 5.93	0.87 ± 0.69	0.02 ± 0.36
NGC 0001	10.84	0.57	9.87 ± 0.02	SAb	SF	MS	SF	2.01 ± 0.28	2.6 ± 0.47	2.25 ± 0.33	0.39 ± 0.15
NGC 0155	11.08	−1.51	<7.45	S0	⋯	RS	fR	⋯	⋯	⋯	⋯
NGC 0169	11.24	0.73	9.54 ± 0.01	SAab	LINER	MS	MX	⋯	⋯	⋯	⋯
NGC 0171	10.77	−0.12	8.98 ± 0.02	SBab	⋯	GV	cQ	6.94 ± 4.06	4.94 ± 1.06	1.27 ± 0.44	0.15 ± 0.05
NGC 0180	11.08	0.21	9.62 ± 0.02	SBbc	⋯	MS	QnR	8.50 ± 3.90	10.16 ± 2.15	1.74 ± 0.60	0.12 ± 0.05
NGC 0693	9.84	−0.65	6.86 ± 0.02	S0/a	⋯	MS	SF	⋯	⋯	⋯	⋯
NGC 0731	10.94	−1.55	<6.84	E	⋯	RS	fR	⋯	⋯	⋯	⋯
NGC 0768	10.86	0.27	9.25 ± 0.02	SBbc	⋯	MS	SF	7.92 ± 2.74	17.97 ± 6.58	1.87 ± 0.60	0.13 ± 0.09
NGC 0955	10.11	−1.08	6.53 ± 0.04	Sab	⋯	GV	nR	⋯	⋯	⋯	⋯
NGC 1056	10.28	0.16	8.6 ± 0.01	Sa	SF	MS	SF	1.47 ± 1.20	2.66 ± 3.95	0.56 ± 0.12	0.08 ± 0.04
NGC 1542	10.57	−0.03	6.34 ± 0.47	Sab	SF	MS	MX	⋯	⋯	⋯	⋯
NGC 2449	11.13	−0.2	9.03 ± 0.02	Sab	LINER	GV	MX	6.97 ± 10.57	4.63 ± 2.16	0.72 ± 0.27	0.03 ± 0.16
NGC 2540	10.54	0.11	9.47 ± 0.03	SBcd	⋯	MS	SF	4.23 ± 0.42	8.09 ± 1.54	0.74 ± 0.56	0.02 ± 0.37
NGC 2554	11.11	0.68	9.4 ± 0.02	S0/a	AGN	MS	nR	3.89 ± 0.43	3.85 ± 0.68	5.25 ± 0.51	0.47 ± 0.35
NGC 2595	10.9	0.12	9.57 ± 0.02	SABc	⋯	MS	QnR	2.96 ± 0.19	7.07 ± 1.45	2.17 ± 0.75	0.24 ± 0.03
NGC 2596	10.76	0.26	9.13 ± 0.02	Sb	⋯	MS	SF	4.84 ± 0.80	12.95 ± 6.32	3.07 ± 0.46	0.16 ± 0.07
NGC 3300	10.76	−1.75	<6.84	SAB	⋯	RS	fR	⋯	⋯	⋯	⋯
NGC 6427	10.63	−1.85	7.39 ± 0.17	S0-	⋯	RS	fR	1.51 ± 0.57	⋯	0.97 ± 0.19	0.14 ± 0.05
NGC 7025	11.17	0.23	<7.6	Sa	LINER	MS	nR	⋯	⋯	⋯	⋯
NGC 7194	11.25	−1.14	<7.86	E	LINER	RS	fR	⋯	⋯	⋯	⋯
NGC 7311	11.12	0.36	9.1 ± 0.02	Sab	LINER	MS	cQ	2.77 ± 0.58	⋯	0.99 ± 0.31	0.06 ± 0.14
NGC 7321	11.13	0.53	9.41 ± 0.02	SBb	LINER	MS	QnR	4.86 ± 1.02	6.8 ± 1.15	0.72 ± 0.61	0.02 ± 0.41
NGC 7364	11.18	0.66	9.58 ± 0.02	S0/a	⋯	MS	SF	2.18 ± 0.29	2.76 ± 0.47	5.55 ± 0.35	0.75 ± 0.47
NGC 7466	10.95	0.36	9.56 ± 0.02	Sb	AGN	MS	SF	4.05 ± 0.38	6.91 ± 1.10	1.51 ± 0.56	0.10 ± 0.13
NGC 7489	10.83	0.54	9.42 ± 0.02	Sd	SF	MS	SF	5.27 ± 0.64	9.78 ± 2.21	1.68 ± 0.57	0.07 ± 0.11
NGC 7625	10.32	0.21	9.33 ± 0.02	SAa	SF	MS	SF	1.13 ± 0.81	0.74 ± 0.35	0.14 ± 0.11	0.01 ± 0.43
NGC 7716	10.69	−0.18	7.86 ± 0.08	SABb	⋯	GV	cQ	1.69 ± 0.90	⋯	0.69 ± 0.25	0.20 ± 0.10
UGC 00312	10.13	0.24	8.42 ± 0.06	SBd	SF	MS	SF	4.45 ± 1.09	8.72 ± 4.18	1.08 ± 0.37	0.04 ± 0.14
UGC 00335 NED 02	10.66	−1.26	<7.58	E	LINER	RS	nR	⋯	⋯	⋯	⋯
UGC 01123	10.73	−0.87	<6.73	Sab	⋯	RS	MX	⋯	⋯	⋯	⋯
UGC 01368	11.21	0.53	8.93 ± 0.03	Sab	⋯	MS	SF	⋯	⋯	⋯	⋯
UGC 01938	10.64	0.13	8.68 ± 0.03	Sbc	⋯	MS	SF	⋯	⋯	⋯	⋯
UGC 02099	11.14	−0.49	<7.58	S0	⋯	RS	MX	⋯	⋯	⋯	⋯
UGC 04240	10.98	0.37	9.19 ± 0.02	S	⋯	MS	SF	⋯	⋯	⋯	⋯
UGC 04245	10.54	−0.14	9.02 ± 0.02	SBb	⋯	MS	cQ	6.04 ± 0.95	23.75 ± 14.75	1.45 ± 0.53	0.05 ± 0.14
UGC 04455	11.5	0.26	<7.51	SBa	⋯	GV	cQ	⋯	⋯	⋯	⋯
UGC 05396	10.81	0.23	8.36 ± 0.05	Scd	SF	MS	SF	⋯	⋯	⋯	⋯

Table 2
(Continued)

Name	log[$M_\star$] ($M_\odot$)	log[SFR] ($M_\odot$ yr^{-1})	log[$M_{\rm mol}$] ($M_\odot$)	Morph. Class	Nuclear	ΔSFR Class	Quenching Stage	$l_\star$ (kpc)	$l_{\rm CO}$ (kpc)	$R_{\rm b}$ (kpc)	$M_{\rm b}$ ($M_\odot/M_\star$)
(1)	(2)	(3)	(4)	(5)	(6)	(7)	(8)	(9)	(10)	(11)	(12)
UGC 08322	11.15	0.06	8.67 ± 0.05	Sa	⋯	GV	MX	⋯	⋯	⋯	⋯
UGC 08781	11.09	0.37	8.65 ± 0.13	SBb	LINER	MS	cQ	7.29 ± 1.59	⋯	7.10 ± 0.67	0.23 ± 0.12
UGC 10972	10.75	−0.19	8.26 ± 0.058	Scd	LINER	GV	cQ	⋯	⋯	⋯	⋯
UGC 11649	10.57	−0.47	7.76 ± 0.19	SBa	LINER	GV	MX	6.12 ± 3.30	⋯	4.45 ± 0.42	0.08 ± 0.05
UGC 11680 NED 02	11.17	1.0	9.82 ± 0.02	E	AGN	MS	SF	1.55 ± 0.17	1.95 ± 0.18	2.64 ± 0.54	0.52 ± 0.12
UGC 11717	11.28	0.61	9.6 ± 0.02	Sc	LINER	MS	MX	3.79 ± 0.73	4.36 ± 0.58	0.65 ± 0.52	0.02 ± 0.41
UGC 11792	10.64	0.02	8.67 ± 0.02	Sc	SF	MS	SF	⋯	⋯	⋯	⋯
UGC 11958	11.2	−0.4	<7.22	E	LINER	RS	nR	⋯	⋯	⋯	⋯
UGC 11982	10.04	−0.36	7.53 ± 0.12	SBcd	⋯	MS	SF	⋯	⋯	⋯	⋯
UGC 12224	10.18	−0.3	9.22 ± 0.02	Scd	SF	MS	SF	5.94 ± 1.91	18.32 ± 10.46	0.67 ± 0.54	0.02 ± 0.36
UGC 12250	11.06	0.08	8.65 ± 0.1	SBb	⋯	GV	cQ	10.39 ± 5.26	⋯	1.71 ± 0.57	0.17 ± 0.09
UGC 12274	11.09	−0.69	8.47 ± 0.09	S	LINER	RS	nR	⋯	⋯	⋯	⋯
UGC 12348	11.0	0.81	9.05 ± 0.02	Sa	AGN	MS	MX	⋯	⋯	⋯	⋯
VV 488 NED 02	10.9	0.36	8.43 ± 0.03	SBc	SF	MS	SF	⋯	⋯	⋯	⋯

Note. Column (1): galaxy name. Columns (2) and (3): logarithmic of the total stellar masses and SFRs from CALIFA. Column (4): logarithmic of the total molecular gas mass as derived, explained in Section 3.1. Column (5): morphological classification drawn from NED. Column (6): emission line diagnostics for the optical nucleus spectrum for CALIFA galaxies by García-Lorenzo et al. (2015), who classify them into SF, AGN, and LINER-type galaxies. These groups are also complemented by the type I and type II AGN classification by Lacerda et al. (2020). Column (7): Galaxy classification according to ΔSFR as explained in Section 4.1.1: main sequence (MS), green valley (GV), and red cloud (RS). Column (8): Two-dimensional emission line classification from Kalinova et al. (2021, 2022), who classify galaxies as SF, quiescent nuclear ring (QnR), centrally quiescent (cQ), mixed (MX), nearly retired (nR), and fully retired (fR). Columns (9) and (10): exponential scale lengths of the molecular gas and stars, respectively, as derived in Section 4.1.2. Columns (11) and (12): radius and mass of bulges, as derived in Section 3.3.

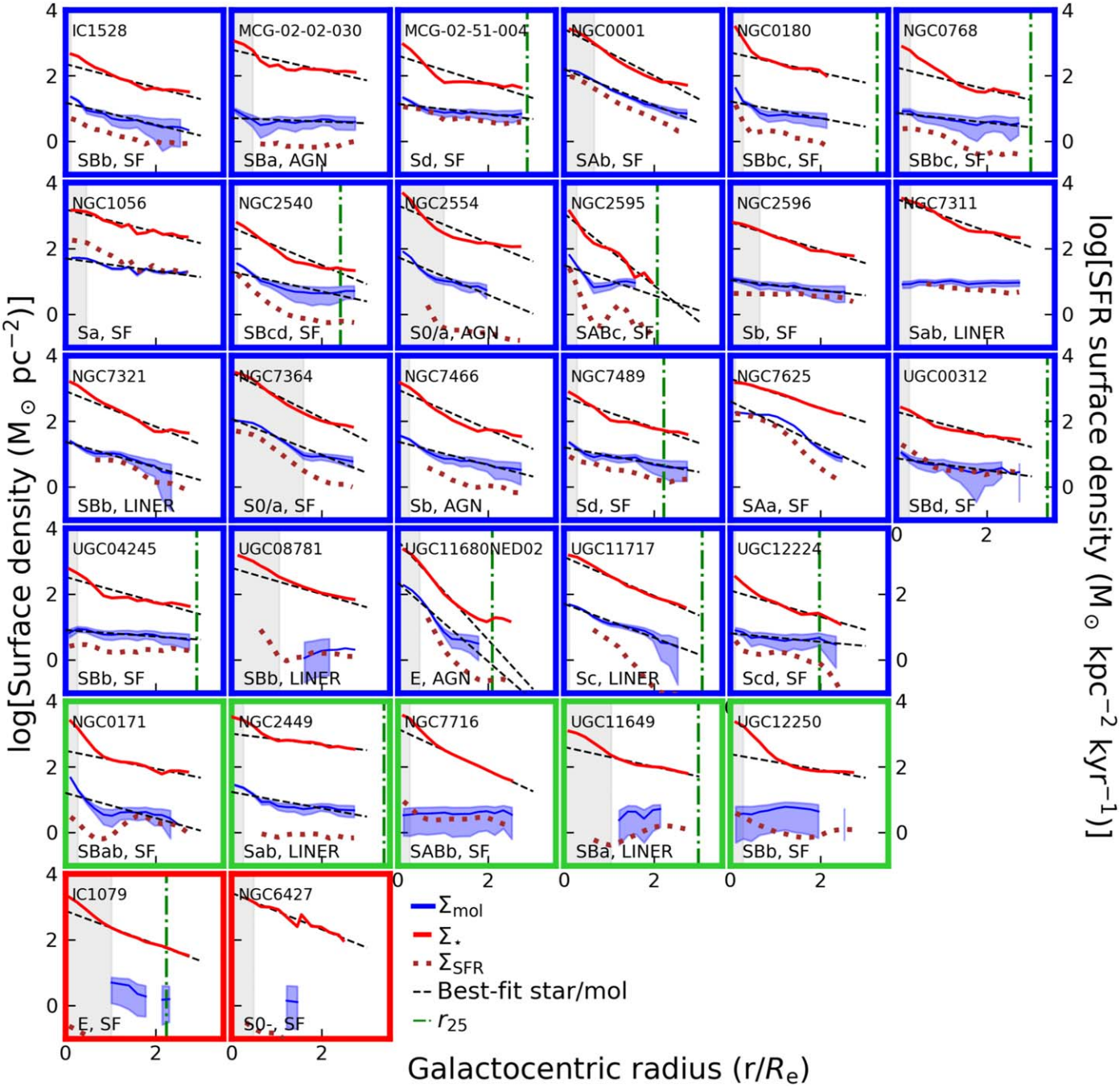

Figure 6. Stellar ($\Sigma_\star$; red solid line) and molecular gas ($\Sigma_{\rm mol}$; blue solid line) surface densities, in units of $M_\odot$ pc^{-2}, as a function of galactocentric radius, in units of the stellar effective radius (R_e), for the 30 ACA EDGE galaxies with 5σ CO detections and inclinations $i \leqslant 70°$. The blue shaded area is the $\pm 1\sigma$ uncertainty. The brown dotted line is the SFR surface density, $\Sigma_{\rm SFR}$. The gray shaded area is the region within the bulge radius, $R_{\rm bulge}$. Dashed black lines correspond to the best exponential function fit for stellar and molecular gas radial profiles, from top to bottom. The dashed–dotted green line corresponds to $r = r_{25}$. The code in the bottom left corner corresponds to the Hubble type and the nuclear activity (columns (5) and (6) in Table 2, respectively). SFRs at $r < 0.5R_e$ have been removed for LINER and AGN galaxies, since Hα in this region is susceptible to LINER/AGN contamination (see Section 4.2.2). Galaxies are classified based on their ΔSFMS as defined in Section 4.1, i.e., in the main sequence (blue panels), green valley (green panels), and red cloud (red panels). When using stellar profiles as a benchmark, we note a systematic flattening of the molecular gas profiles with ΔSFMS. See also Figure 12.

4.1. Global Quantities and Relations

4.1.1. SFR versus Stellar and Molecular Gas Masses

The top left panel of Figure 7 shows the SFR–$M_\star$ relation, color-coded by $M_{\rm mol}$, using the global values (pixels at $r < r_{25}$) of SFR and $M_\star$ (see Section 3.1). On average, we note that galaxies near the SFMS (black line; Cano-Díaz et al. 2016) tend to have higher molecular gas masses, although there is no clear region on the SFR–$M_\star$ relation associated with low values of $M_{\rm mol}$ (see color-coded symbols). In order to characterize the behavior of the molecular gas as a function of the difference between the SFR and the SFMS, ΔSFMS = log[SFR] − SFMS, we classify our galaxies into three different groups based on their ΔSFMS, as shown by the shaded areas in the top left panel of Figure 7.

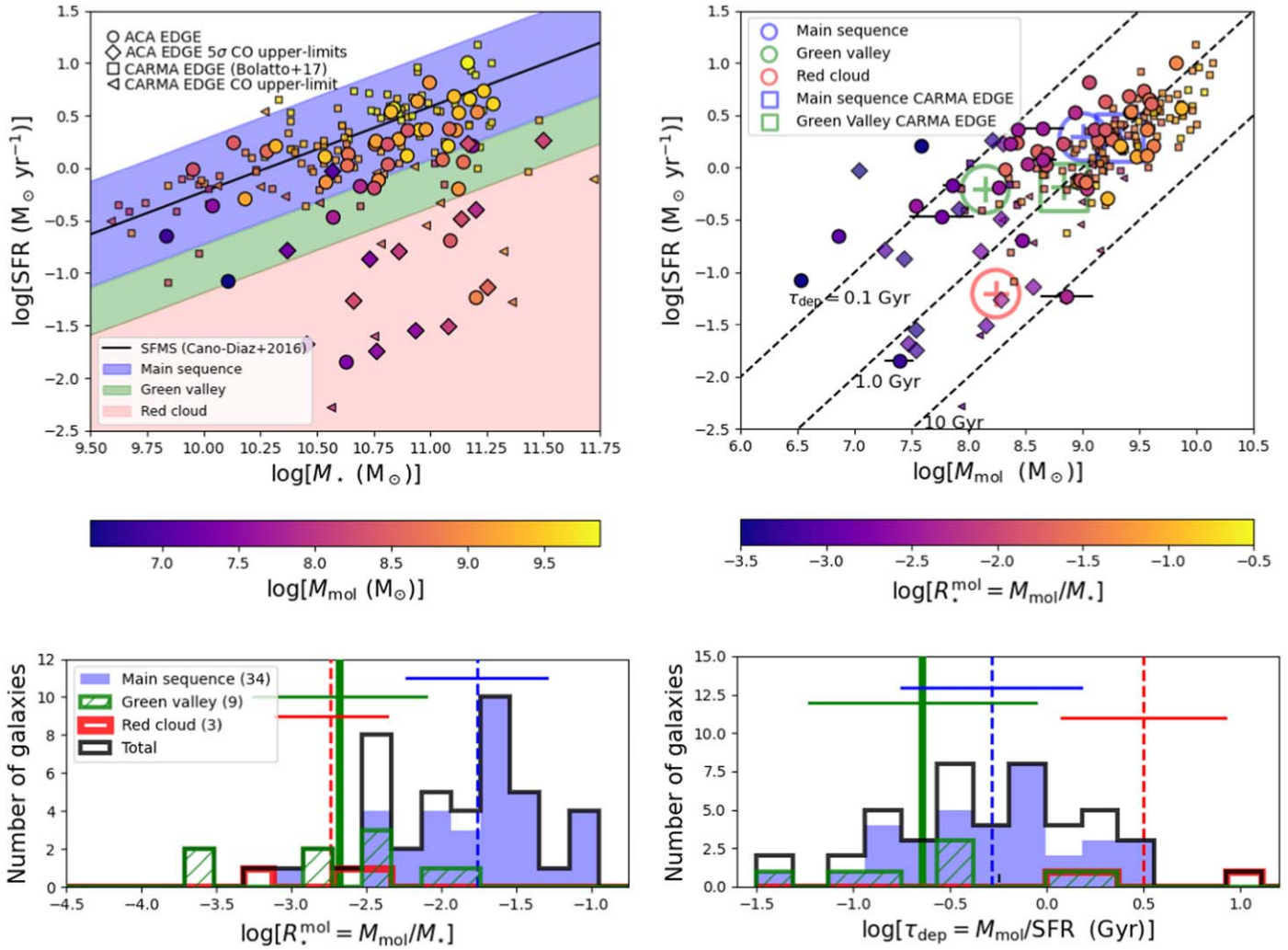

Figure 7. Top left: SFR–$M_\star$ diagram integrated over CALIFA SFR and stellar maps, color-coded by the total molecular gas mass, $M_{\rm mol}$. The solid black line is the SFMS fit by Cano-Díaz et al. (2016). Blue, green, and red shaded areas define main-sequence, green valley, and red cloud galaxies, respectively, as defined by the bands (see Section 4.1 for more details). Top right: SFR–$M_{\rm mol}$ relation color-coded by stellar mass. The dashed black lines, from top to bottom, correspond to molecular gas depletion times $\tau_{\rm dep} = 0.1$, 1.0, and 10 Gyr, respectively. Blue, green, and red circles are the centroids of SFR and $M_{\rm mol}$ values for galaxies with 5σ CO detections (filled circles) of the groups as defined by the bands in the top left panel. The blue and green squares correspond to the centroid of SFR and $M_{\rm mol}$ values for main-sequence and green valley CARMA EDGE–detected galaxies. Bottom: distributions for the molecular-to-stellar mass fraction ($R_\star^{\rm mol} = M_{\rm mol}/M_\star$; left) and the molecular gas depletion time ($\tau_{\rm mol} = M_{\rm mol}/{\rm SFR}$; right) for the three categories (excluding CO upper limits) as defined in top left panel. Vertical and horizontal lines correspond to the average values and the standard deviations of the distributions, respectively. The plots suggest that while the transition from main-sequence to green valley galaxies is mostly driven by gas removal/depletion, the movement from the latter to the red cloud may be determined by a reduction in the SFE of the molecular gas (${\rm SFE}_{\rm mol} = \tau_{\rm dep}^{-1}$).

1. Main sequence (36 galaxies, 34 with 5σ CO detections; blue shaded area), which are galaxies with $-0.5\,{\rm dex} < \Delta{\rm SFMS}$.
2. Green valley (11 galaxies, 9 with 5σ CO detections; green shaded area), encompassing galaxies with $-1.0\,{\rm dex} < \Delta{\rm SFMS} \leqslant -0.5\,{\rm dex}$.
3. Red cloud (13 galaxies, 3 with 5σ CO detections; red shaded area), which includes galaxies with $\Delta{\rm SFMS} \leqslant -1.0\,{\rm dex}$.

We choose these boundaries based on the typical values of the main-sequence/green valley distribution scatters reported in recent studies, which span from ∼0.2 to 0.7 dex (e.g., Schawinski et al. 2014; Chang et al. 2015; Bland-Hawthorn & Gerhard 2016; Cano-Díaz et al. 2016; Sánchez et al. 2018; Colombo et al. 2020). The bottom left panel of Figure 7 shows the distribution of the molecular-to-stellar mass fraction, $R_\star^{\rm mol} = M_{\rm mol}/M_\star$, of the three groups for galaxies with 5σ CO detections. Main-sequence galaxies have the highest molecular gas masses (with an average $\log[R_\star^{\rm mol}] \sim -1.6$ dex; blue dashed line), while on average, both green valley and red cloud galaxies have fractions about an order of magnitude lower (green solid and red dashed lines).

The top right panel of Figure 7 shows the SFR–$M_{\rm mol}$ relation, color-coded by $M_\star$. The three dashed black lines correspond to three different molecular depletion times, $\tau_{\rm dep} = M_{\rm mol}/{\rm SFR} = 0.1$, 1.0, and 10 Gyr, going from top to bottom, respectively. It is interesting to note that although most ACA EDGE galaxies are well represented by the $\tau_{\rm dep} = 1$ Gyr line, there is no characteristic molecular depletion time for the whole sample. This is confirmed when we analyze the molecular gas depletion time distributions of the three groups (bottom right panel of Figure 7); red cloud galaxies have a $\tau_{\rm dep}$ around 3 and 6 times longer than main-sequence and green valley galaxies, respectively. However, these results have to be

considered carefully due to the small number of CO-detected red cloud galaxies.

Our results are consistent with Colombo et al. (2020), who analyze ^{12}CO($J = 2-1$) APEX data at 26.″3 resolution (i.e., the region within R_e) for 472 EDGE galaxies. They note a strong correlation between ΔSFMS and the SFE of the molecular gas, $SFE_{mol} = \tau_{dep}^{-1}$, suggesting a scenario where the transition of galaxies from the main sequence to the green valley is primarily driven by the molecular gas lost. In addition, they propose that changes in the SFE_{mol} of the remaining cold gas are what modulate a galaxy's retirement from the green valley to the red cloud. Analyzing a compilation of ∼8000 galaxies from MaNGA, Sánchez et al. (2018) also note that the SFE decreases as galaxies move out of the main sequence to the red cloud and pass through the green valley, which is confirmed by several studies (e.g., Brownson et al. 2020; Sánchez 2020; Sánchez et al. 2021; Lin et al. 2022).

4.1.2. Exponential Scale Lengths

If gas removal/depletion is one of the main processes modulating the transition from main-sequence to green valley galaxies, it should impact the distribution of the molecular gas. To test this, we compute the exponential scale lengths for the molecular gas, l_{mol}, and the stars, $l_\star$, for the ACA EDGE galaxies in Figure 6. Figure 8 shows the comparison between l_{mol} and $l_\star$ for main-sequence ACA EDGE galaxies with $i < 70°$ and 5σ CO detections (see Section 3.2). Galaxies are color-coded by their ΔSFMS according to the classification explained in Figure 7. Out of the 30 galaxies with molecular gas and stellar radial profiles, we have selected 23 galaxies with decreasing Σ_{mol} profiles (i.e., $\Sigma_{mol}(r < 1\ \mathrm{kpc}) > \Sigma_{mol}(r = r_{max})$, where r_{max} is the largest radius at which we have a 5σ CO detection). Since we also restrict the $\Sigma_\star(r)$ exponential fit to the stellar disk, we do not consider annuli within prominent bulges (i.e., E and S0 galaxies; Regan et al. 2001) and bars (i.e., SB, Sab, and Sbc galaxies). These fits for Σ_{mol} and $\Sigma_\star$ profiles are shown by the black dashed lines in Figure 6. We observe a significant correlation between l_{mol} and $l_\star$ for main-sequence and green valley galaxies (blue and green circles; Pearson $r_p = 0.6$, p-value < 0.01). When we compute an ordinary least-squares (OLS; blue solid line in Figure 8) bisector fit for the model $y = \alpha x$ for main-sequence galaxies with at least 5σ l_{mol} measurements (symbols with darker color in Figure 8), we obtain $l_{mol} = (1.24 \pm 0.05) \times l_\star$. We test how this relation varies with angular resolution by fitting the CO radial profiles derived from CO moment 0 maps smoothed at 10″ beam size. Although molecular length scales are slightly larger than for stars $l_{mol} = (1.15 \pm 0.05) \times l_\star$, the best linear relation is still above unity.

While several studies have found a close 1:1 relation between the molecular gas and stars in main-sequence SF galaxy samples based on galaxies selected from the field (e.g., Young et al. 1995; BIMA, Regan et al. 2001; HERACLES, Leroy et al. 2008; CARMA EDGE, Bolatto et al. 2017; Villanueva et al. 2021), quenching mechanisms have the potential to affect the distribution of the molecular gas, atomic gas, and stars in different ways. On the one hand, environmental mechanisms (e.g., ram pressure stripping and galaxy interactions, among others) have been shown to compact the spatial extent of the molecular gas, particularly in high-density environments (e.g., galaxy clusters; Boselli et al. 2014; Zabel et al. 2022). For instance, Villanueva et al. (2022) find a ∼3:5 relation for the molecular and stellar scale lengths in a subsample of 28 Virgo cluster galaxies selected from VERTICO (Brown et al. 2021). On the other hand, intrinsic mechanisms tend to operate either by removing (e.g., via AGN activity), redistributing (e.g., via stellar feedback), or depleting (e.g., via starvation) the cold gas reservoirs. Figure 6 shows a broad variety of radial profiles that could be explained by a different combination of mechanisms depending on the galaxy ΔSFMS. The best relation between molecular gas and stellar scale length for ACA EDGE main-sequence galaxies (blue circles in Figure 8) is close to a 6:5 relation. Although this is still consistent with the almost ∼1:1 relation from Villanueva et al. (2021), l_{mol} values for ACA EDGE galaxies are slightly larger when compared to CARMA EDGE spirals. This seems to be the result of the lower molecular gas content in the central regions of the former rather than the latter (as shown by the M_{mol} centroids in top right panel of Figure 7). This, in consequence, produces flatter Σ_{mol} profiles in ACA EDGE galaxies than those for CARMA EDGE, which were mainly selected to be bright in the far-IR (i.e., rich in molecular gas; see Section 2.1 and Bolatto et al. 2017 for more details).

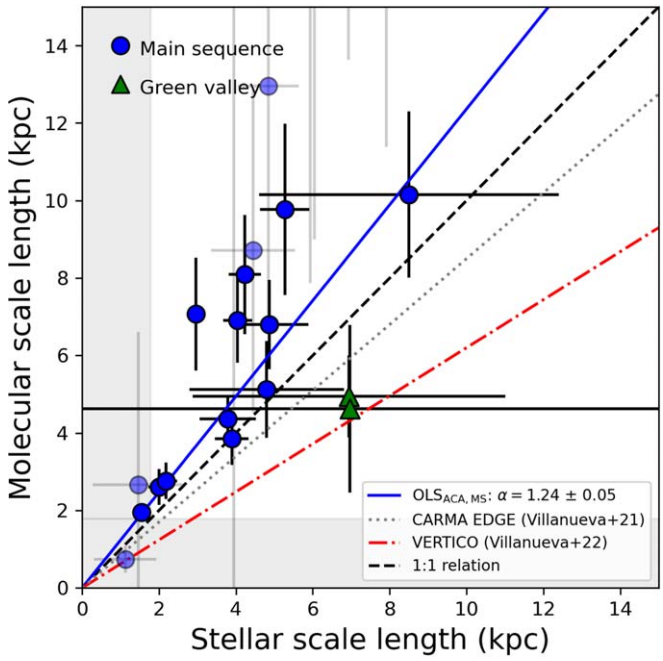

Figure 8. Comparison between the stellar, $l_\star$, and molecular, l_{mol}, scale lengths, computed by fitting exponential profiles to the respective surface densities as a function of galactocentric radius. Blue circles and green triangles correspond to 23 ACA EDGE galaxies with $\Sigma_{mol} > 1\ M_\odot\ \mathrm{pc}^{-2}$ for all the annuli within 1 kpc. The blue solid line is the best fit for the model $y = \alpha x$ for the main sequence, omitting galaxies with low-quality l_{mol} fits (light-colored symbols). The gray dotted and orange dashed–dotted lines are the best-fit relation for CARMA EDGE (Villanueva et al. 2021) and VERTICO (Villanueva et al. 2022), respectively. The shaded gray area corresponds to the median physical resolution of ACA EDGE galaxies. On average, the figure shows a ∼6:5 relation between the molecular and stellar scale lengths.

4.2. Spatially Resolved Relations

4.2.1. SFR versus Stellar and Molecular Gas Surface Densities

The left panel of Figure 9 shows Σ_{SFR} versus $\Sigma_\star$ (the so-called resolved SFMS, rSFMS; e.g., Cano-Díaz et al. 2016; Lin et al. 2019; Ellison et al. 2021a; Sánchez et al. 2021c), both in units of

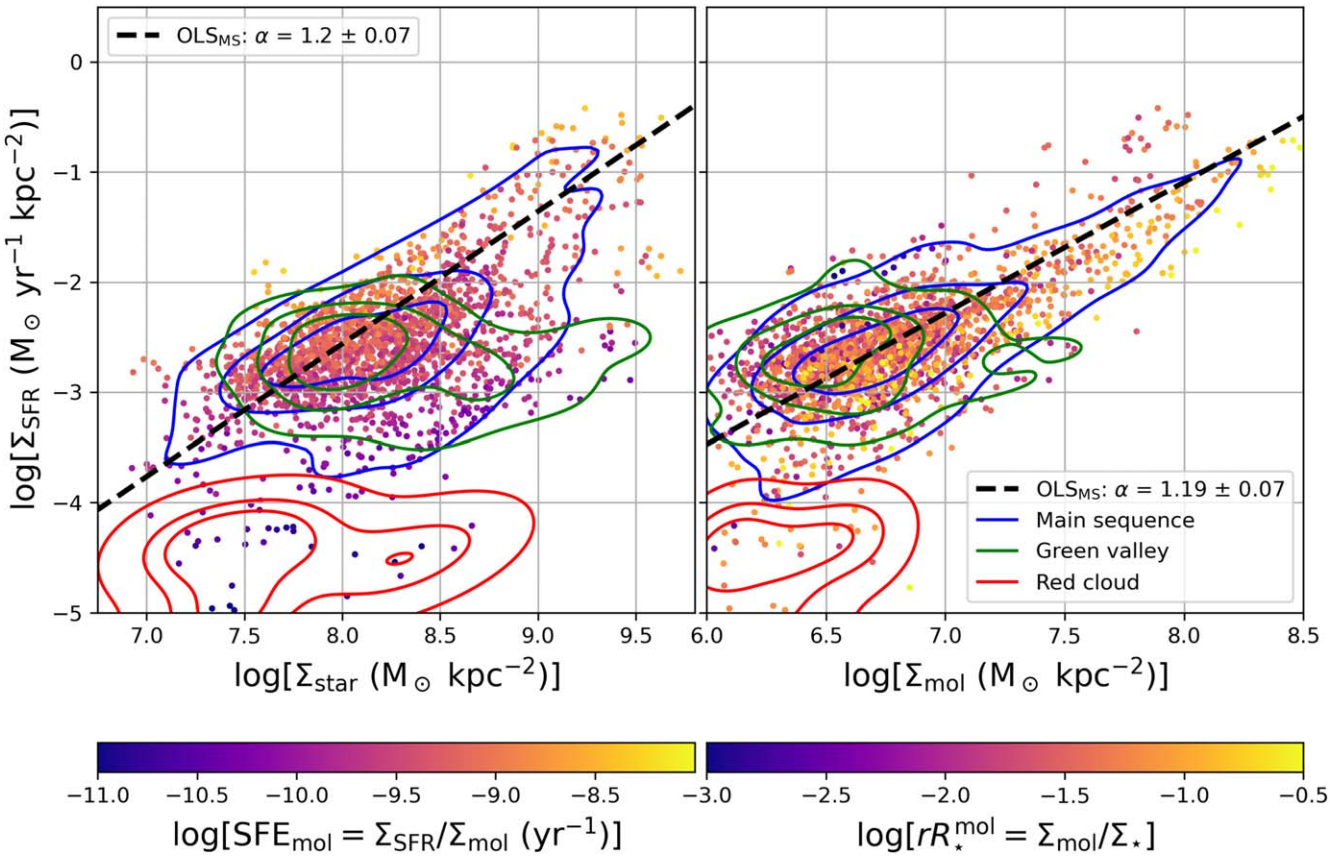

Figure 9. Left: SFR surface density, Σ_{SFR}, vs. stellar surface density, $\Sigma_\star$, color-coded by the resolved SFE of the molecular gas, SFE = $\Sigma_{SFR}/\Sigma_{mol}$, for pixels with 5$\sigma$ CO detections and selected from the 30 galaxies included in Figure 6. Blue and green density contours are 90%, 60%, and 30% of the points for main-sequence and green valley galaxies. Right: the resolved SFR–M_{mol} relation, color-coded by the resolved molecular-to-stellar mass gas fraction, $rR_\star^{mol} = \Sigma_{mol}/\Sigma_\star$. Conventions are the same as in the left panel. The black dashed lines correspond to the OLS bisector fit for main-sequence galaxies using the model $y = \alpha x + \beta$ for the rSFMS (left) and the rKS (right) relations. While the left panel exhibits an increase in $\Sigma_\star$ for pixels transiting from the main sequence to the green valley, the right panel shows that pixels from these two populations cover a similar parameter space, although with a mild decrease in Σ_{SFR}. This suggests that changes in star formation activity during the transition are driven not only by a lowering of the molecular gas but also a decrease of the SFE.

$M_\odot$ kpc^{-2} and color-coded by the resolved SFE of the molecular gas, SFE$_{mol}$ = $\Sigma_{SFR}/\Sigma_{mol}$. The figure includes pixels from the 30 ACA EDGE galaxies with 5σ global CO detections and $i < 70°$. Similar to Section 4.1, we classify pixels according to the ΔSFMS of the host galaxy as main sequence (blue contours), green valley (green contours), and red cloud (red contours). Although there is not a remarkable difference in the $\Sigma_\star$ range covered by the main-sequence and green valley pixels, there is a mild decrease in Σ_{SFR} from the former (log[Σ_{SFR}] ∼ −2.7 dex) to the latter (log[Σ_{SFR}] ∼ −3.0 dex). However, red cloud pixels have the lowest SFR of all groups. To compare our results with previous studies, we compute an OLS bisector fit for main-sequence pixels using the model $y = \alpha x + \beta$; we obtain log[Σ_{SFR}] = (1.20 ± 0.07) × log[$\Sigma_\star$] − (12.18 ± 0.60) (dashed black line in left panel of Figure 9). Our rSFMS best-fit slope, α_{rSFMS}, is slightly higher than those for CARMA EDGE ($\alpha_{rSFMS} \approx 1.01$; Bolatto et al. 2017), PHANGS ($\alpha_{rSFMS} \approx 1.04$; Pessa et al. 2021), and other galaxy sample (see Sánchez et al. 2023 and references therein). However, our results are consistent with the values found in several studies based on galaxy samples similar to ACA EDGE (e.g., Lin et al. 2019). For instance, Ellison et al. (2021a) analyze the rSFMS properties of ∼15,000 spaxels in a sample of 29 galaxies selected from the ALMA-MaNGA QUEnching and STar formation (ALMaQUEST) survey (Lin et al. 2020). Covering the same range of stellar masses, ALMaQUEST was designed to investigate the star formation activity in galaxies from the green valley to the starburst regime, complementing surveys with a better representation of galaxy properties in the local Universe (e.g., CARMA EDGE). Implementing an orthogonal distance regression (ODR) fit for the rSFMS, Ellison et al. (2021a) find log[Σ_{SFR}] = (1.37 ± 0.01) × log[$\Sigma_\star$] − (13.12 ± 0.10), resulting in a steeper rSFMS slope (clearly above unity) for high stellar mass galaxies.

Similar to the rSFMS, the widely studied resolved Kennicutt–Schmidt (rKS) relation (e.g., Bigiel et al. 2008; Leroy et al. 2008; Schruba et al. 2011; Pessa et al. 2021; Sánchez et al. 2021; Jiménez-Donaire et al. 2023; Sun et al. 2023) presents a complementary way to investigate how the SFR depends on the ISM. The right panel of Figure 9 contains the rKS relation for ACA EDGE galaxies, color-coded by the resolved molecular-to-stellar mass fraction, $rR_\star^{mol} = \Sigma_{mol}/\Sigma_\star$, and density contours as in the left panel. It is interesting to note that the OLS bisector fit for main-sequence galaxies also yields an rKS best-fit slope value, α_{rKS}, above unity (log[Σ_{SFR}] = (1.19 ± 0.07) × log[Σ_{mol}] − (10.62 ± 0.98); dashed black line in right panel of Figure 9). Although our α_{rKS} is higher when compared to that for CARMA EDGE ($\alpha_{rKS} \approx 1.01$; Bolatto et al. 2017), PHANGS ($\alpha_{rKS} \approx 1.03$; Pessa et al. 2021), and other galaxy samples from the literature (see Sánchez et al. 2023 and references therein), it is consistent with the ODR fit for ALMaQUEST galaxies (log[Σ_{SFR}] = (1.23 ± 0.01) × log[Σ_{mol}] − (10.49 ± 0.06); Ellison et al. 2021a). We note, however, that these results are very sensitive to the adopted

α_{CO} prescription. For instance, Sun et al. (2023) show that different assumptions of the CO-to-H_2 conversion factor can result in $\alpha_{rKS} = 0.9$–1.2, which translates into uncertainties up to 25% in the CO-related quantities of PHANGS galaxies. We also observe a systematic decrease in both Σ_{SFR} and Σ_{mol} from the main sequence to the green valley galaxies. In combination with the results shown in the left panel, this may suggest that although the transition from the main sequence to the green valley is primarily driven by gas removal, a decrease in SFE_{mol} also plays a role in modifying the ability of the molecular gas to form stars (see the color-coded points in the left panel of Figure 9).

4.2.2. SFE and Bulge Properties

To understand which mechanisms may be driving the star formation quenching in ACA EDGE galaxies, we analyze the impact of bulges on the SFE of the molecular gas. It is important to mention that SFR estimators derived from Hα have to be taken carefully, since they are susceptible to contamination due to AGN activity, jets, shocks and post–asymptotic giant branch stars (Lacerda et al. 2020). To perform our analysis only on SF pixels, we have used estimates of the nuclear activity of CALIFA galaxies from García-Lorenzo et al. (2015; column (5) in Table 2), who classify galaxies according to the emission line diagnostic of the optical nucleus in SF, AGN, and LINER-type galaxies. Although recent studies have proposed the term "LIERs" (or "low ionization emission regions") to redefine the term "LINER," (or "low ionization nuclear emission-line regions") since the latter is not only limited to nuclear regions neither restricted to galaxy centers (e.g., Singh et al. 2013; Belfiore et al. 2016), for simplicity, we use the term LINER. We complement the AGN classification using Lacerda et al. (2020), who group CALIFA galaxies as type I (galaxies with a broad Hα width, i.e., FWHM $>$ 1000 km s^{-1}) or type II (galaxies above the Kewley et al. 2001 line on the BPT diagram and Hα line width $>$3Å) AGNs. Although galaxies may host an AGN and actively form stars, we classify galaxies as SF if no nuclear activity is detected. We adopt this since we do not see significant variations between the results for confirmed SF-only galaxies and SF+not-detected nuclear activity galaxies.

The top panel of Figure 10 shows the resolved SFE_{mol} as a function of galactocentric radius (in units of r_{25}), color-coded by the ΔSFMS of the host galaxy, for SF pixels within R_b. The figure also includes the SFE_{mol} pixels within the centers (including the bulge and nucleus) of PHANGS–ALMA galaxies drawn from Querejeta et al. (2021; black plus signs), which complement the ACA EDGE sample by providing data at smaller galactocentric radii. On average, ACA EDGE green valley pixels have lower efficiencies compared to those for PHANGS and ACA EDGE main-sequence galaxies, with the latter two covering a similar range of SFE_{mol}. To test how these results depend on the α_{CO} prescription, we compute the SFE_{mol} by adopting a variable $\alpha_{CO}(Z', \Sigma_{total})$ (see Equation (6)), as shown in the top panel of Figure 10 by dashed contours. On average, $\alpha_{CO}(Z', \Sigma_{total})$ values are lower than for the fixed prescription at $r \lesssim 1.5R_e$; consequently, SFE_{mol} are higher when derived from $\alpha_{CO}(Z', \Sigma_{total})$. We note that green valley galaxies have a slightly higher increase in the efficiencies than main-sequence galaxies (∼0.3 dex) with the variable α_{CO}, although with the former still having lower SFE_{mol} than the latter. The middle panel of Figure 10 shows the SFE_{mol} as a function of the sSFR, $sSFR = \Sigma_{SFR}/\Sigma_\star$, for ACA EDGE pixels

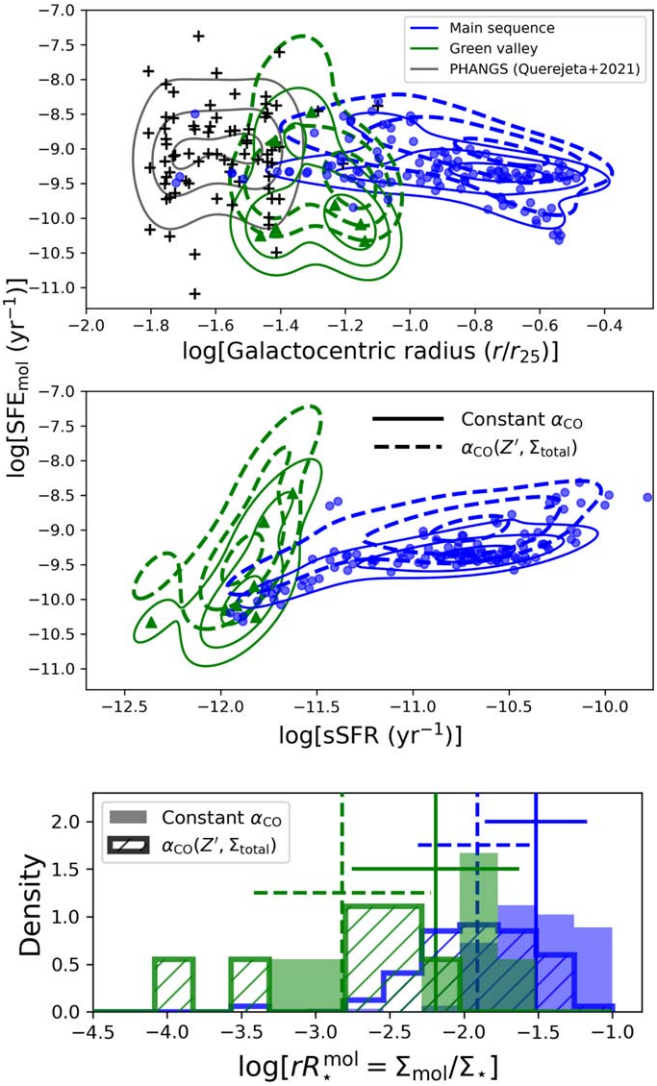

Figure 10. Top: the resolved SFE_{mol} vs. galactocentric radius for SF pixels within R_b, color-coded by their ΔSFMS. Black plus signs are pixels drawn for PHANGS–ALMA spirals. Solid blue and green lines correspond to 90%, 60%, and 30% density contours of main-sequence and green valley pixels, respectively. Dashed lines are density contours for pixels when adopting a variable $\alpha_{CO}(Z', \Sigma_{total})$ prescription (see Equation (6)). Middle: the resolved SFE_{mol} vs. the resolved sSFR for the same groups as in the top panel. Bottom: distribution of the resolved molecular-to-stellar mass fraction, $rR_\star^{mol}$, for main-sequence and green valley galaxies included in the top panel. The vertical and horizontal lines are the mean and standard deviation values of the distributions, respectively. We note that the spatially resolved SFE_{mol}, sSFR, and $rR_\star^{mol}$ within the bulges have a systematic decrease with ΔSFMS, and these trends seem to not depend on the adopted α_{CO} prescription.

within the bulge region. We note a systematic increase of the efficiencies with the sSFR, going from low SFE_{mol} values for green valley galaxies ($\log[SFE_{mol}] \sim -10.3$ and $\log[sSFR] \sim -12$) to high SFE_{mol} values for main-sequence galaxies ($\log[SFE_{mol}] \sim -9.3$ and $\log[sSFR] \sim -10.5$). Even though efficiencies are higher when compared to those derived from the fixed α_{CO}, these tendencies do not change when adopting the variable α_{CO} prescription (as shown by dashed contours in the top and middle panels of Figure 10). These results are in agreement with several studies reporting lower star formation efficiencies in bulge-dominated galaxies (e.g., Colombo et al. 2018; Ellison et al. 2021b; Sánchez et al. 2021). For instance, Catalán-Torrecilla et al. (2017) report a decrease in the SFRs

with sSFR within bulges of CALIFA galaxies at any $M_\star$. Eales et al. (2020) also find a clear correlation between the SFE and sSFR in galaxies without prominent bulges and with the same morphological type. In addition, they note a strong connection between massive bulges and low SFE.

Are the differences in $\mathrm{SFE_{mol}}$ between main-sequence and green valley bulges primarily driven by gas depletion/removal? To test this, we compute the resolved molecular-to-stellar mass fraction, $rR_\star^{\mathrm{mol}} = \Sigma_{\mathrm{mol}}/\Sigma_\star$, for pixels within the bulge region from these two groups. The bottom panel of Figure 10 shows the distribution of $rR_\star^{\mathrm{mol}}$ of pixels within bulges and adopting the fixed (hatched histograms) and variable (solid histograms) α_{CO} prescriptions. On average, $rR_\star^{\mathrm{mol}}$ values of green valley pixels are ∼3 times lower than those within main-sequence bulges when adopting the fixed α_{CO}. Although we note a displacement to the left of the mean $rR_\star^{\mathrm{mol}}$ values of the pixel distributions when adopting the variable α_{CO}, the tendencies do not change significantly ($rR_\star^{\mathrm{mol}}$ values for green valley galaxies are ∼5 times lower than for main-sequence galaxies).

Similarly to the morphological quenching proposed by Martig et al. (2009), numerical simulations performed by Gensior et al. (2020) show that bulges drive turbulence and increase the gas velocity dispersion, σ_{gas}; virial parameter; and turbulent pressure, P_{turb}, toward the galaxy centers. They note that the more compact and more massive (and therefore more dense) the bulges are, the higher the level of turbulence. The star formation activity is, therefore, "dynamically suppressed" in the innermost parts of bulge-dominant galaxies due to an increase of the gas turbulence that prevents the gravitational instabilities. Figure 11 shows the distribution of the bulge density, ρ_{b}, for main-sequence and green valley galaxies. To compute ρ_{b}, we assume a spheroidal distribution of the bulge; i.e., we use $\rho_{\mathrm{b}} = M_{\mathrm{b}}/(\frac{4}{3}\pi R_{\mathrm{b}}^3)$. Although green valley galaxies are poorly represented, Figure 11 shows that, on average, green valley bulges tend to be denser than those for main-sequence galaxies. These results suggest that, when compared to main-sequence pixels, the lower $\mathrm{SFE_{mol}}$ values within green valley bulges are not just a consequence of poor molecular gas content. In addition, dynamical suppression may be reducing the SFR in these regions due to an increase in $\Sigma_\star$ with ΔSFMS (green valley bulges are ∼3 times denser than those of main-sequence galaxies).

Which quenching mechanism is more important? In agreement with our results, recent studies support the idea that changes in both the gas reservoir and efficiency are responsible for reduced star formation in the disk of green valley galaxies. For instance, analyzing CO(1−0) data from the NOrthern Extended Millimeter Array and ALMA for seven nearby green valley galaxies, Brownson et al. (2020) show that the efficiency of star formation at their centers is, on average, 3 times lower than expected from the rKS (with some galaxies even up to 10 times less efficient). However, when they compare the resolved molecular gas main sequence (rMGMS; $\Sigma_\star$–Σ_{mol}) and the rKS relations, they note that neither changes in the efficiency nor gas content dominate at $r \gtrsim 0.6R_{\mathrm{e}}$. They conclude that while offsets from the rMGMS appear to dominate in the central regions, the full extent of the corresponding offsets from the rKS is unconstrained and makes them unable to rank the two drivers in these regions. Similar results are shown by Lin et al. (2022), who analyze the quenching mechanism in 22 green valley and 12 main-sequence galaxies selected from ALMaQUEST. They note that the reduction of SFE and $R_\star^{\mathrm{mol}}$ in green valley galaxies (relative to main-sequence galaxies) is seen in both bulge and disk regions (although with larger uncertainties). Their results thus suggest that, statistically, quenching in green valley galaxies may persist from the inner to the outer regions, and also that both gas depletion/removal and dynamical suppression are equally important.

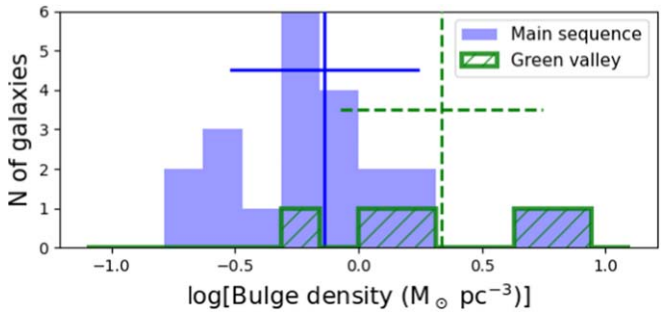

Figure 11. Distributions of the bulge density (in units of $M_\odot$ pc^{-3}) for the 23 main-sequence and five green valley galaxies included in Figure 6. The vertical and horizontal lines are the mean and standard deviation values of the distributions, respectively. Although we do not see a statistically significant difference between green valley and main-sequence bulge densities, we note that the former have, on average, denser bulges than the latter.

4.2.3. What Drives Star Formation Quenching in ACA EDGE Galaxies?

The six panels in Figure 12 show the resolved $\mathrm{SFE_{mol}}$ (top panels), $rR_\star^{\mathrm{mol}}$ (middle panels), and sSFR, $\mathrm{sSFR} = \Sigma_{\mathrm{SFR}}/\Sigma_\star$ (bottom panels) versus galactocentric radius (in radial bins of $0.3R_{\mathrm{e}}$, ∼1.5 kpc resolution at the mean distance) for the 30 galaxies included in Figure 6 (i.e., the 30 ACA EDGE galaxies with $i < 70°$ and 5σ CO detections). In order to better understand the different mechanisms behind star formation quenching in ACA EDGE galaxies, we split the panels of Figure 12 into two groups. Panels (A), (C), and (E) include SF galaxies (hereafter no nuclear activity, NNA, galaxies; i.e., pixels from galaxies without LINER/AGN activity), split by their ΔSFMS (i.e., main sequence, green valley, and red cloud). Panels (B), (D), and (F) include pixels from NNA, LINER, and AGN galaxies (shaded purple, orange, and yellow regions, respectively) according to their nuclear activity (column (5) in Table 2).

On average, the $\mathrm{SFE_{mol}}$ remains almost constant with radius for NNA main-sequence, green valley, and red cloud galaxies (panel (A)). These results are consistent with Villanueva et al. (2021); while they do not observe significant variations of $\mathrm{SFE_{mol}}$ with radius in the CARMA EDGE sample, they also note a systematic decrease in the efficiencies from late- to early-type galaxies. In addition, panel (A) shows that green valley galaxies have a mild increase in $\mathrm{SFE_{mol}}$ with radius. While main-sequence and green valley galaxies have similar $rR_\star^{\mathrm{mol}}$ for $r \gtrsim 1.8R_{\mathrm{e}}$ (see panel (C)), the latter have significantly lower $rR_\star^{\mathrm{mol}}$ than the former at $r \lesssim 1.5R_{\mathrm{e}}$. Molecular-to-stellar mass fractions for green valley galaxies can reach values ∼0.8 dex below those for main-sequence galaxies at $r \lesssim 0.5R_{\mathrm{e}}$. Similarly, sSFRs show almost the same radial trends as $rR_\star^{\mathrm{mol}}$ (see panel (E)). The sSFR values in green valley galaxies are typically about an order of magnitude below those of main-sequence galaxies (∼1.2 dex). These results suggest that what is driving the star formation quenching in green valley galaxies is related to both a decrease of the SFR (e.g., via changes in the SFE) and gas removal and/or depletion.

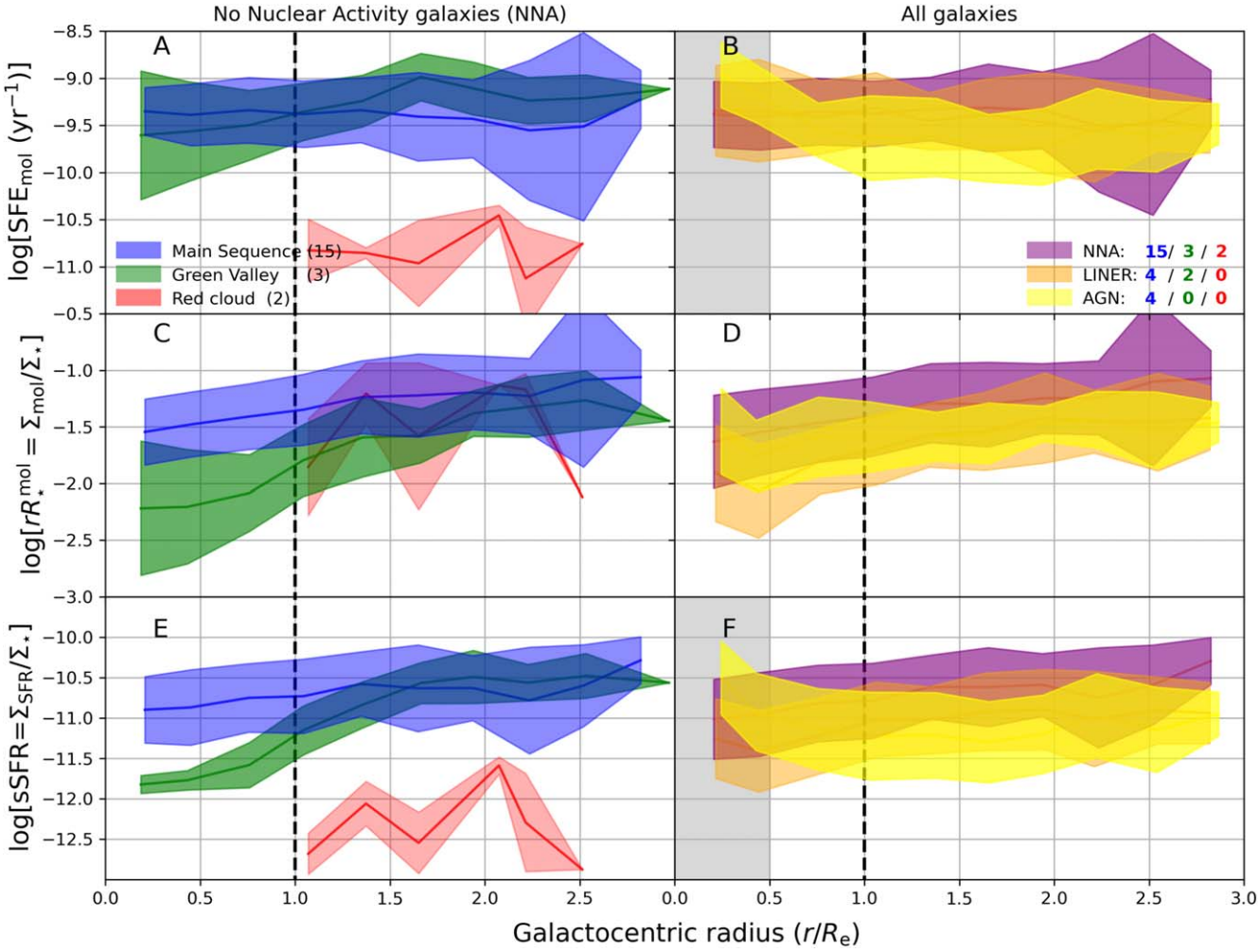

Figure 12. The resolved SFE of the molecular gas, $\mathrm{SFE_{mol}} = \Sigma_{\mathrm{SFR}}/\Sigma_{\mathrm{mol}}$ (panels (A) and (B)); the resolved molecular-to-stellar mass fraction, $rR_{\star}^{\mathrm{mol}} = \Sigma_{\mathrm{mol}}/\Sigma_{\star}$ (panels (C) and (D)); and the sSFR, $\mathrm{sSFR} = \Sigma_{\mathrm{SFR}}/\Sigma_{\star}$ (panels (E) and (F)) in radial bins of $0.3R_{\mathrm{e}}$ ($\sim$1.5 kpc) vs. galactocentric radius for pixels from the 30 galaxies included in Figure 6. The figure is color-coded according to the three main groups. Panels (A), (C), and (E) encompass pixels from 20 galaxies classified as SF (or with NNA; see column (5) in Table 2), split by the ΔSFMS (i.e., main sequence, green valley, and red cloud) of the host galaxy. Panels (B), (D), and (F) include pixels from 30 ACA EDGE galaxies grouped according to the nuclear activity of the host galaxy. The gray shaded areas correspond to the regions where our Hα-based SFR estimator is susceptible to AGN/LINER contamination, so SFR and related quantities are only taken as upper limits. In all panels, the vertical extent of the shaded areas is the 1σ scatter distribution for any group. Also, the vertical black dashed lines are located at $r = R_{\mathrm{e}}$, which we use to divide galaxy regions in central and disk pixels. While efficiencies in main-sequence galaxies remain almost constant with galactocentric radius, in green valley galaxies, we note a systematic increase of $\mathrm{SFE_{mol}}$, $rR_{\star}^{\mathrm{mol}}$, and sSFR with increasing radius. We also observe slightly higher $\mathrm{SFE_{mol}}$ in the regions near the centers ($0.5R_{\mathrm{e}} \lesssim r \lesssim 1.2R_{\mathrm{e}}$) of AGNs when compared to their outskirts.

Similar to panel (A) of Figure 12, panel (B) shows that NNA galaxies (mostly dominated by the main sequence) have, on average, flat $\mathrm{SFE_{mol}}$ profiles. Although both LINER and AGN galaxies have remarkably high efficiencies in the central regions ($r \lesssim 0.5R_{\mathrm{e}}$; gray shaded area in panels (B) and (F)), these values have to be considered carefully due to LINER/AGN contamination (as explained in Section 4.2.2). Consequently, $\mathrm{SFE_{mol}}$ (and related quantities) must be considered only as upper limits for these two groups within this region. While LINERs and SFs show a flat $\mathrm{SFE_{mol}}$ profile for $r \gtrsim 0.5R_{\mathrm{e}}$, AGNs seem to have significantly lower efficiencies in the range $0.75R_{\mathrm{e}} \lesssim r \lesssim 2.0R_{\mathrm{e}}$ than LINER/NNA galaxies, which finally flatten at larger galactocentric radii. When analyzing $rR_{\star}^{\mathrm{mol}}$ as a function of galactocentric radius (shown in panel (D)), we observe a systematic inside-out increase of the molecular fractions with radius for each of the three groups. However, LINERs/AGNs have $rR_{\star}^{\mathrm{mol}}$ values slightly lower than NNA galaxies ($\sim$0.2–0.5 dex below) for the galactocentric radius range covered here. We also note that, on average, sSFR has a similar behavior as $\mathrm{SFE_{mol}}$, particularly for AGN galaxies that show a slight decrease of the sSFR with radius (similar to the one seen for $\mathrm{SFE_{mol}}$). This may be suggesting that AGN activity mitigates the star formation activity, although not necessarily by impacting the H_2 reservoirs (e.g., Bluck et al. 2020a, 2020b).

Our results are consistent with CALIFA-based studies reporting lower molecular gas fractions in the centers of AGN-hosting galaxies when compared to their outskirts (e.g., Sánchez et al. 2018; Lacerda et al. 2020; Ellison et al. 2021b). However, observational evidence has also shown that the gas content in AGN hosts can be similar (or even higher) than galaxies without nuclear activity by analyzing either the atomic (e.g., Ho et al. 2008; Fabello et al. 2011; Ellison et al. 2019) or molecular (e.g., Maiolino et al. 1997; Saintonge et al. 2017; Koss et al. 2021; Esposito et al. 2022) gas reservoirs.

These results suggest that the cessation of the star formation activity has different modes depending on galaxy substructure, morphological type, and nuclear activity. NNA main-sequence and

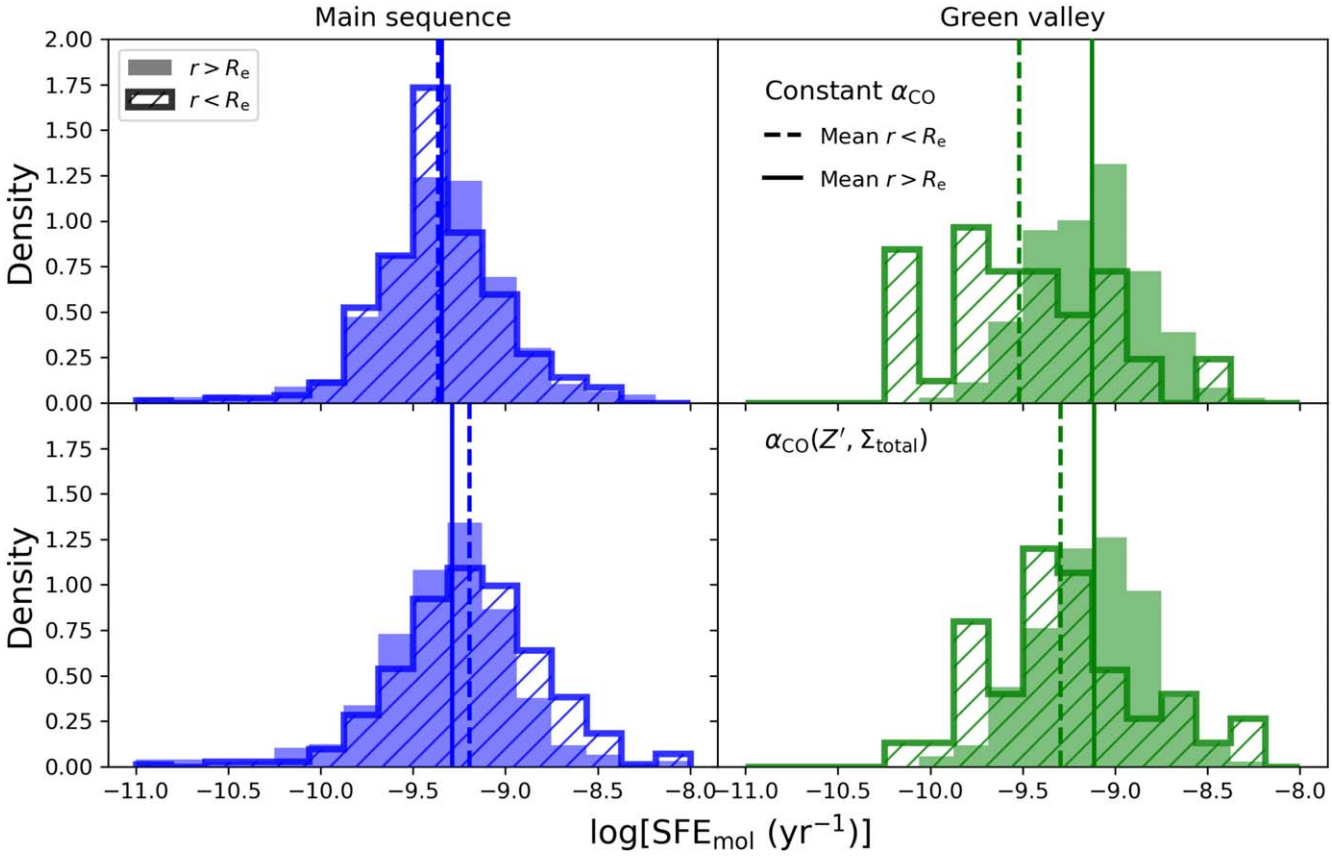

Figure 13. SFE_{mol} distributions for pixels from NNA galaxies, split into main-sequence (blue bars) and green valley (green bars) galaxies (left and right panels, respectively). The two groups are split by two radial bins according to the breaks identified in Figure 12 and thus between pixels within the central (hatched open bars) and outer (solid bars) regions. To compute the SFE_{mol}, we adopt a fixed CO-to-H_2 conversion factor (top panels) and the variable $\alpha_{CO}(Z', \Sigma_{total})$ from Equation (6) (bottom panels). While the distributions of SFE_{mol} for main-sequences pixels within the two radial bins are similar when adopting the two α_{CO} prescriptions, green valleys show a clearer bimodal behavior when using a constant α_{CO}.

green valley galaxies have SFE_{mol} consistent with local SF spirals (e.g., Villanueva et al. 2021, 2022), which, on average, remain constant with radius. Nevertheless, green valley galaxies show signs of an inside-out increase in their efficiencies. To better understand these differences, we compute the SFE distributions for NNA galaxies by splitting them into central pixels (i.e., pixels at $r < R_e$) and outer pixels (i.e., pixels at $r > R_e$). We also test how these distributions change with the two α_{CO} prescriptions included in this work (as shown in Figure 13). The distribution of SFE_{mol} for main-sequence galaxies is almost identical when we split their pixels into two radial bins at $r = R_e$. If we adopt a fixed α_{CO} (top panels), green valley and red cloud pixels show a clear bimodal behavior. We test how the SFE distributions change by using the variable $\alpha_{CO}(Z', \Sigma_{total})$ prescription (bottom panels). Interestingly, we note that green valley galaxies show mild bimodal distributions. We perform a Student's t-test to verify if the distribution of SFE_{mol} values in green valley galaxies is drawn from the same parent population. We obtain $|t| = 0.89$ for green valley (degrees of freedom = 222) pixel distributions, which is below the critical t-value $t_{\alpha=0.05} \approx 1.96$; we thus can reject the null hypothesis that the two green valley groups are drawn from the same underlying distribution with 95% confidence. Although these results suggest that morphological quenching may be acting after the gas removal stage in green valley galaxies (e.g., Colombo et al. 2020), the small difference between these two distributions may be caused by the poor spatial resolution of our CO observations (~1.5 kpc) when compared to the physical scale required to resolve bulges in ACA EDGE galaxies ($\lesssim$500 pc). In addition, some studies (e.g., Cook et al. 2019, 2020) have discarded a scenario where bulges play a key role in controlling the star formation activity, suggesting that this could be reflecting physical processes more associated with galaxy disks. Finally, when analyzing the individual SFE_{mol} pixel distributions within R_e for the three green valley galaxies included in the left panels of Figure 13 and using the morphological and bar classification included in Kalinova et al. (2021) for CALIFA galaxies, we note that spiral galaxies without bars (i.e., NGC 7716) seem to have higher efficiencies than those with a predominant bar on their disks (i.e., UGC 12250 and NGC 0171). However, due to the limited galaxy sample included in this analysis, it is essential that future ACA EDGE survey studies increase the green valley coverage to derive more statistically significant conclusions about how structural components (e.g., bars) could enhance the effects of morphological quenching.

Similar to Figure 13, Figure 14 includes the SFE_{mol} distributions for two radial bins, i.e., for pixels within $r < 1.2R_e$ (hatched histograms) and at $r > 1.2R_e$ (solid histograms), in NNA (purple bars), LINER (orange bars), and AGN (yellow bars) galaxies. We also test how the distributions change with the two α_{CO} prescriptions. To avoid SFR contamination due to AGNs/LINERs, we reject pixels at $r < 0.5R_e$. While NNA, LINER, and AGN pixels have similar distributions for the two radial bins and using the fixed α_{CO} (top panels of Figure 14), we note signs of a bimodal behavior for AGNs if we adopt the variable $\alpha_{CO}(Z', \Sigma_{total})$ prescription (bottom left panel). We perform a Student's t-test to verify if

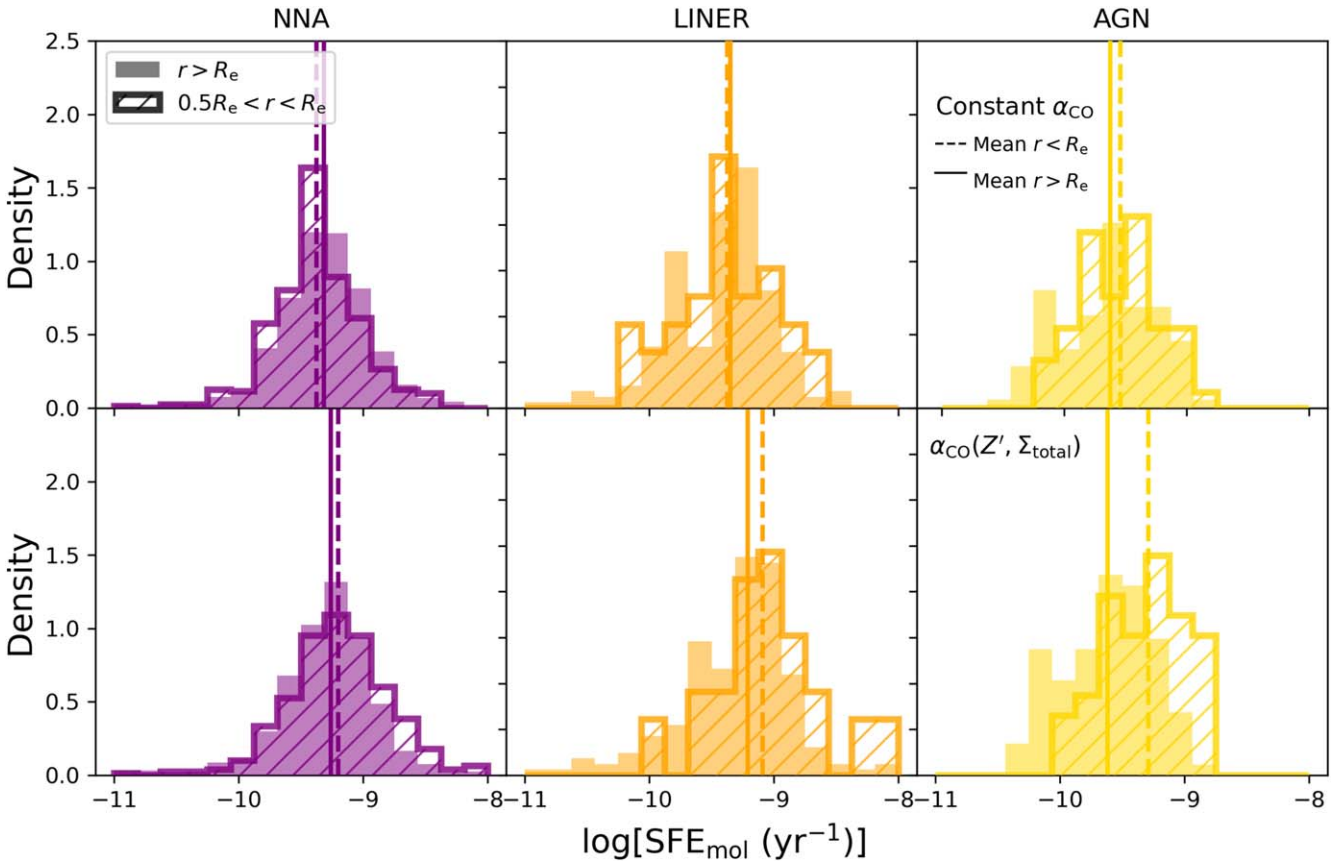

Figure 14. SFE_{mol} distributions for pixels from SF (i.e., galaxies with NNA; purple bars), LINER (orange bars), and AGN (yellow bars) galaxies (from left to right). Conventions are the same as in Figure 13. While NNA and LINER pixels have similar SFE_{mol} distributions for the two radial bins and when testing the two α_{CO} prescriptions, we note a mild bimodal behavior for AGNs.

the AGN distributions are drawn from the same parent population; we obtain $|t| = 1.89$ (degrees of freedom = 140), which is lower than the critical t-value $t_{\alpha=0.05} \approx 1.97$. We thus can reject the null hypothesis that the two AGN groups are drawn from the same underlying distribution. Although SFE_{mol} values for AGNs are consistent with observational evidence showing that optical and radio-selected AGNs tend to have similar/lower SFRs than typical main-sequence galaxies (e.g., Ellison et al. 2016; Sánchez et al. 2018; Lacerda et al. 2020), which appears to be mainly due to the SFR within galaxy centers (e.g., Ellison et al. 2018; Sánchez et al. 2018; Kalinova et al. 2021), these results could also be supporting the idea of a slight enhancement of the star formation in these regions. However, studies have shown that the impact of AGN ionization can reach as far out as tens of kpc (e.g., Veilleux et al. 2003; Husemann et al. 2008; Nesvadba et al. 2011). Although unlikely, we cannot rule out that the high SFEs we measure at the centers of ACA EDGE AGNs are due to contamination by AGN emission, even though we have excluded pixels with $r < 0.5R_e$.

Morphological quenching has been shown to be a good candidate to explain the decrease of the SFE_{mol} observed in green valley ACA EDGE galaxies, perhaps via gas stabilization or dynamical suppression (e.g., Martig et al. 2009; Gensior et al. 2020; Gensior & Kruijssen 2021), by increasing the turbulent velocity dispersion of the gas (e.g., Vollmer & Davies 2013), due to a sequence of short-lived AGNs (e.g., Bluck et al. 2020b, 2020a), or a combination of mechanisms (e.g., Lin et al. 2019). However, the similarity of the SFE distributions shown in the bottom panels of Figures 13 and 14 (particularly for green valley galaxies) suggest that these processes have a minimal impact on the efficiencies. These mechanisms seem to respond to non-long-standing processes and may only complement the gas depletion and/or removal. In addition, recent studies have shown that the presence of a classical bulge seems not to be the only necessary condition for morphological quenching in nearby galaxies. For example, Kalinova et al. (2022) find that some galaxies with large central bulges may actually correspond to SF systems; conversely, some galaxies with small spheroids may be quenched. They also note that higher central surface densities ($\sim 10^4\ M_\odot\ pc^{-2}$), no bars, and early-type morphologies (i.e., no tight and prominent spiral arms) seem to be either connected or an additional condition for dynamical suppression in galaxies.

Further studies based on CO data within galaxy centers with both higher resolution and higher sensitivity than those presented in this work (e.g., at physical scales of $\lesssim$500 pc) could give us more information about the dynamical state of the molecular gas within bulges of green valley and red cloud galaxies. These are essential to disentangle the actual connection between the SFE_{mol} and the gravitational stability of the gas or the effects of AGNs in the star formation activity in detail.

5. Summary and Conclusions

We present a systematic study of the SFE and its dependence on other physical parameters in 60 galaxies from the ACA EDGE

survey. We analyze ^{12}CO($J=2-1$) data cubes and optical IFU data from CALIFA. Compared to other local galaxy surveys, ACA EDGE is designed to mitigate selection effects based on CO brightness and morphological type. This results in a less biased galaxy survey and an ideal sample to investigate the effects of star formation quenching on massive local galaxies. We conduct a detailed analysis to characterize the main properties of the molecular gas by deriving global (e.g., integrated masses and SFRs) and resolved quantities out to typical galactocentric radii of $r\approx 3R_e$. We use a constant Milky Way CO-to-H_2 conversion factor, $\alpha_{CO,MW}=4.3\ M_\odot$ (K km s^{-1} pc^2)$^{-1}$ (Walter et al. 2008), and a Rayleigh–Jeans brightness temperature line ratio of $R_{21}=I_{CO(2-1)}/I_{CO(1-0)}\sim 0.65$. We also test the impact of the constant CO-to-H_2 conversion factor adopted in our results by using the variable $\alpha_{CO}(Z', \Sigma_{total})$ from Bolatto et al. (2013). We conduct a systematic analysis to explore molecular and stellar scale lengths, bulge physical properties, molecular-to-stellar mass fractions, and the SFE of the molecular gas in ACA EDGE galaxies to compare them with the current literature. Our main conclusions are enumerated as follows.

1. We compute the molecular depletion times, τ_{dep}, of ACA EDGE galaxies. Although the majority of galaxies have $\tau_{dep}\sim 1$ Gyr, we find that molecular depletion times vary significantly with the distance of the SFR to the SFMS line, ΔSFMS. Classifying galaxies as main-sequence (-0.5 dex $\leqslant$ ΔSFMS $\leqslant 0.5$ dex), green valley (-1.0 dex $<$ ΔSFMS $\leqslant -0.5$ dex), and red cloud (ΔSFMS $\leqslant -1.0$ dex) galaxies, we note a systematic decrease in the molecular-to-stellar mass fraction, $R_\star^{mol}$, and an increase in τ_{dep} with ΔSFMS (see Figure 7).
2. We determine the molecular and stellar exponential disk scale lengths, l_{mol} and $l_\star$, respectively (see Figure 8). We fit an exponential function to 23 molecular gas surface density, Σ_{mol}, and 30 stellar surface density, $\Sigma_\star$, radial profiles from the 30 ACA EDGE galaxies with 5σ CO detections and inclinations of $<70°$. We find a close 6:5 relation between l_{mol} and $l_\star$ ($l_\star=[1.24\pm 0.05]\times l_{mol}$), which is consistent with previous results from the literature for main-sequence spirals (e.g., HERACLES, CARMA EDGE).
3. We derive the Σ_{SFR}–$\Sigma_\star$ and Σ_{SFR}–Σ_{mol} relations for the rSFMS and rKS relations, respectively (see Figure 9). We find slopes of $\alpha_{rSFMS}=[1.20\pm 0.07]$ and $\alpha_{rKS}=[1.19\pm 0.07]$ for the rSFMS and rKS. Although the slopes for ACA EDGE galaxies are larger than those of spiral SF main-sequence galaxies selected from the field (e.g., CARMA EDGE, PHANGS), they are consistent with those found in galaxy surveys that are more oriented to increase the coverage of green valley and red cloud galaxies (e.g., ALMaQUEST). However, we remark that these slopes are very sensitive to the fitting method and the α_{CO} prescription adopted.
4. We compute the resolved SFE of the molecular gas, SFE_{mol}, within the bulge region of 23 main-sequence and five green valley ACA EDGE galaxies. We find that SFE_{mol} values within green valley bulges tend to be lower than those for main-sequence galaxies (∼3 times lower). The results suggest that in addition to poor molecular gas content, dynamical suppression may be reducing the SFR in the bulge region of green valley galaxies due to a decrease in SFE_{mol} with ΔSFMS (see Figure 10).
5. We compute radial profiles for SFE_{mol}, the resolved molecular-to-stellar mass fraction $rR_\star^{mol}=\Sigma_{mol}/\Sigma_\star$, and the resolved sSFR, $sSFR=\Sigma_{SFR}/\Sigma_\star$, for pixels grouped according to their ΔSFMS and nuclear activity (see Figure 12). We note a systematic decrease in SFE_{mol}, $rR_\star^{mol}$, and sSFR with ΔSFMS. We also observe a slight inside-out increase in the efficiencies in green valley galaxies out to $r\approx R_e$; from this point on, SFE_{mol} increases until it reaches similar values to the almost constant values we observe for main-sequence galaxies. Although the efficiencies of green valley galaxy centers are more similar to those of their outer disks when we use the variable $\alpha_{CO}(Z', \Sigma_{total})$ prescription, on average, their SFE_{mol} distributions show lower efficiencies in their central regions when compared to both those for their outskirts (∼2–3 times lower) and the typical values of main-sequence galaxies (∼2 times lower; see Figure 13).

Our results suggest that although gas depletion and/or removal seem to be the most important mechanism behind the cessation of stellar production, they do not completely explain the star formation quenching processes in ACA EDGE galaxies. Complementary mechanisms (such as morphological quenching and/or AGN feedback) are therefore required to change the physical properties of the molecular gas, which could impact its ability to form stars in galaxies transiting through the green valley. The inside-out nature of these processes is reflected by the decrease of SFE_{mol} in the central regions of green valley galaxies, although this change is dependent on the α_{CO} prescription adopted. Future projects should focus on increasing the ETG coverage to improve the statistical significance of these results. In addition, high-resolution CO observations in the central parts of green valley and red cloud galaxies are essential to better understand how these mechanisms may impact the stability of the gas at physical scales comparable to those of molecular clouds ($\lesssim$100 pc).

Acknowledgments

V.V. acknowledges support from the scholarship ANID-FULBRIGHT BIO 2016-56160020 and funding from NRAO Student Observing Support (SOS) - SOSPADA-015 and the ALMA-ANID Postdoctoral Fellowship under award ASTRO21-0062. A.D.B., S.V., and V.V. acknowledge partial support from NSF-AST1615960. R.C.L. acknowledges support for this work provided by a National Science Foundation (NSF) Astronomy and Astrophysics Postdoctoral Fellowship under award AST-2102625. This work is also supported by NSF under awards AST-2307440 and AST-2307441.

Software: Astropy (Astropy Collaboration et al. 2018), MatPlotLib (Hunter 2007), NumPy (Harris et al. 2020), SciPy (Virtanen et al. 2020), seaborn (Waskom 2021), Scikit-learn (Pedregosa et al. 2011).

Appendix

A.1. Multipanel Images

Figures 15–22 in this appendix follow the same format as Figure 3 and show the products for 53 galaxies included in the ACA EDGE survey.

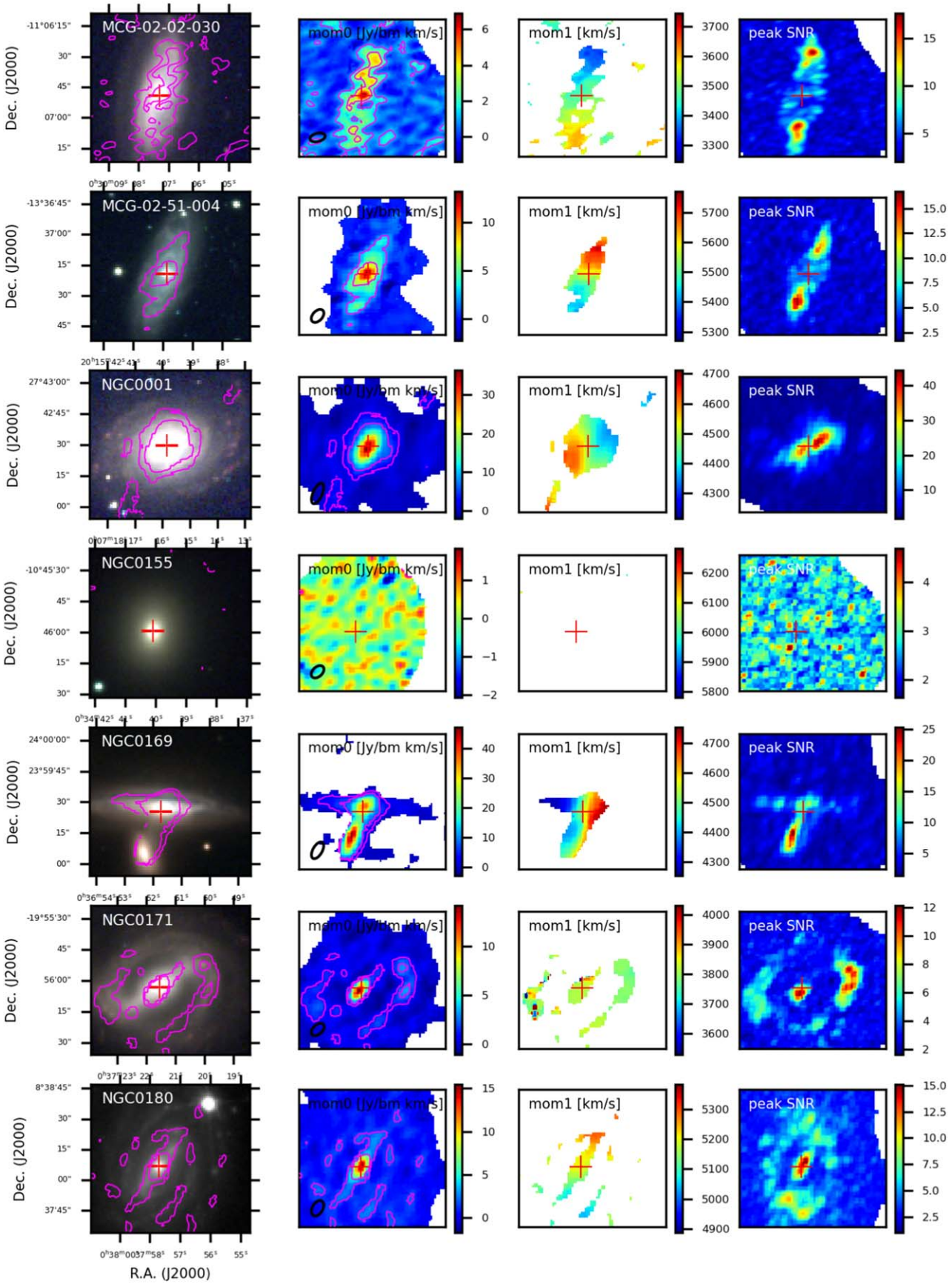

Figure 15. Images for ACA EDGE galaxies. See caption of Figure 3.

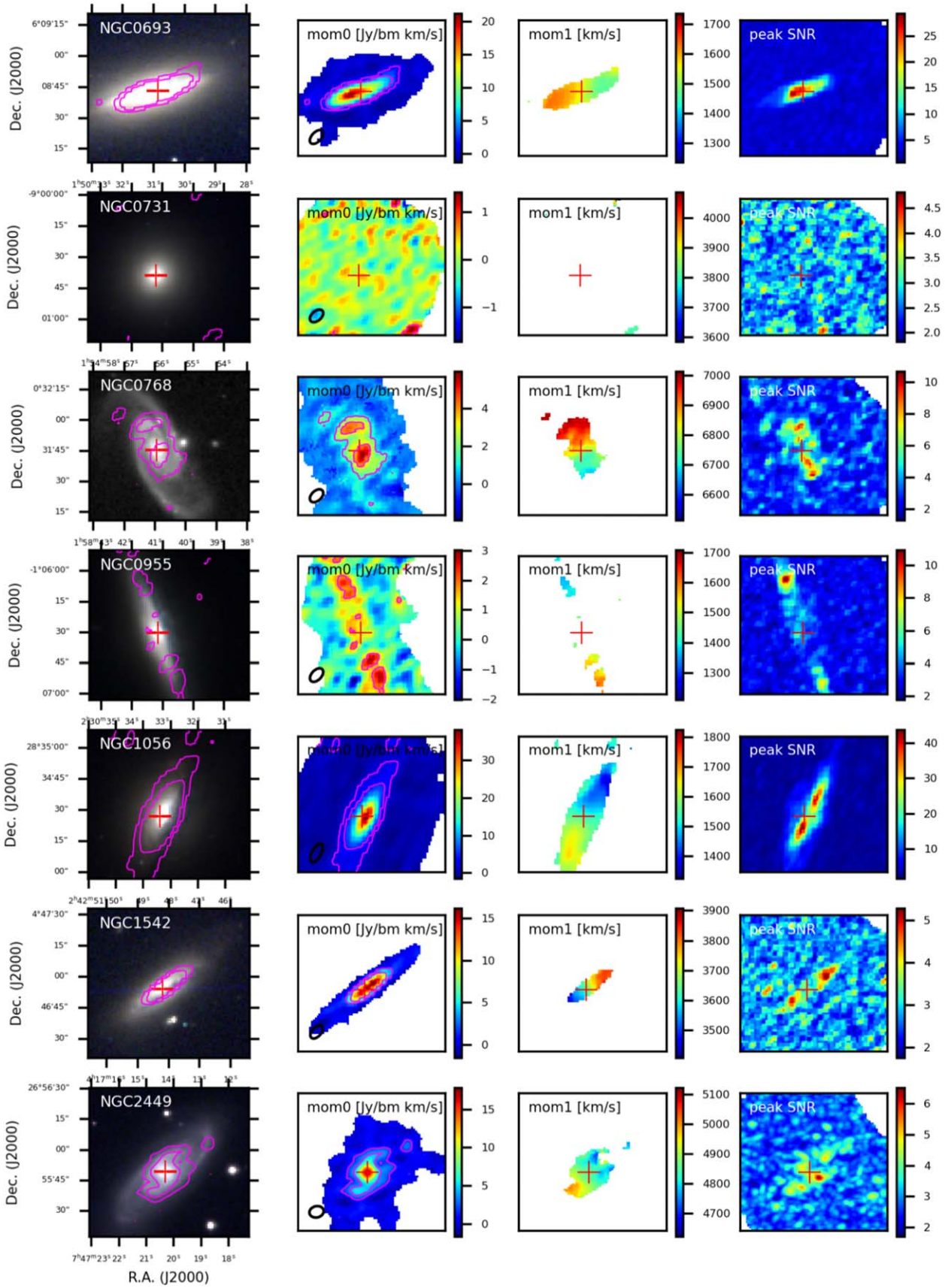

Figure 16. Images for ACA EDGE galaxies. See caption of Figure 3.

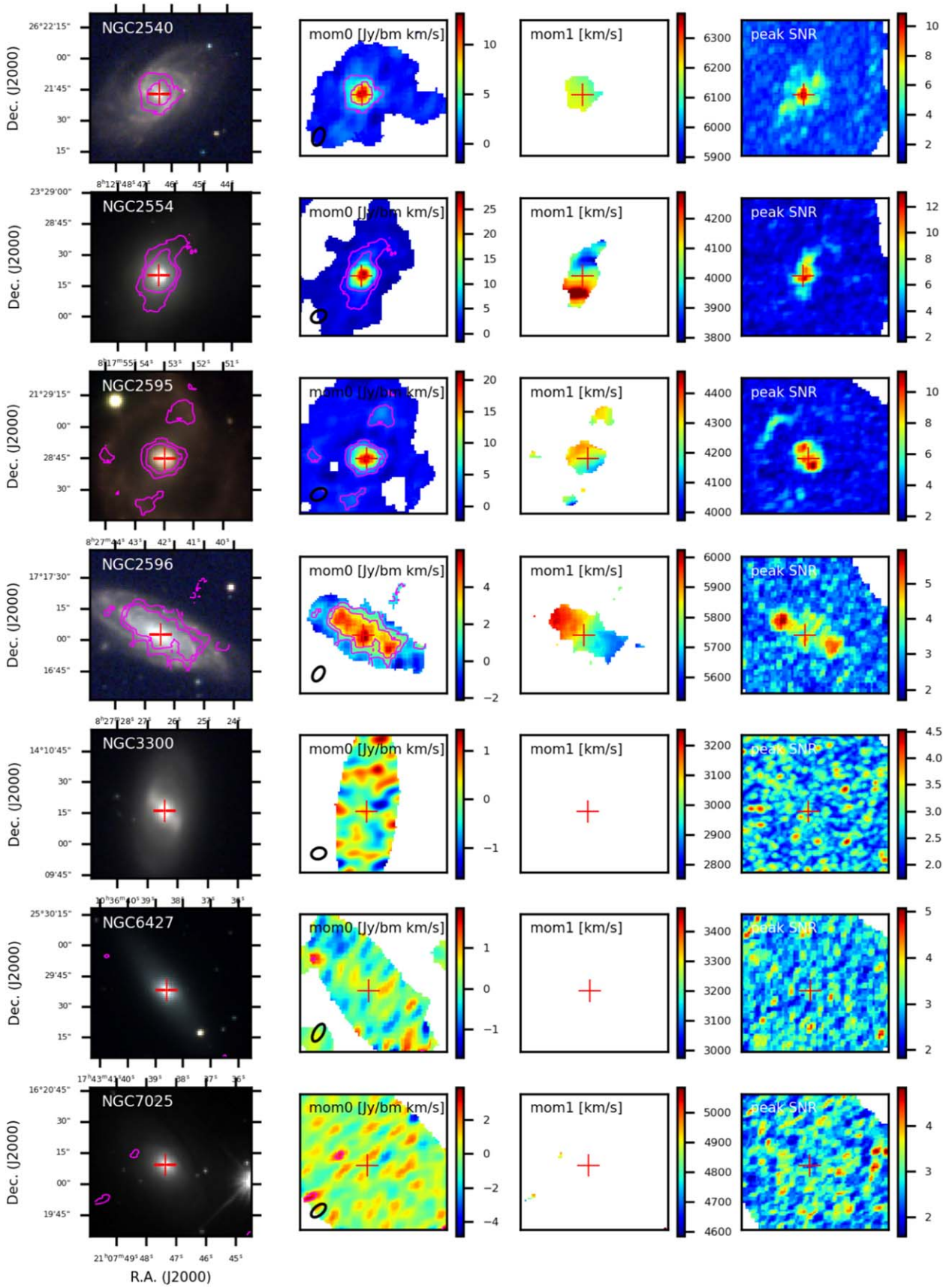

Figure 17. Images for ACA EDGE galaxies. See caption of Figure 3.

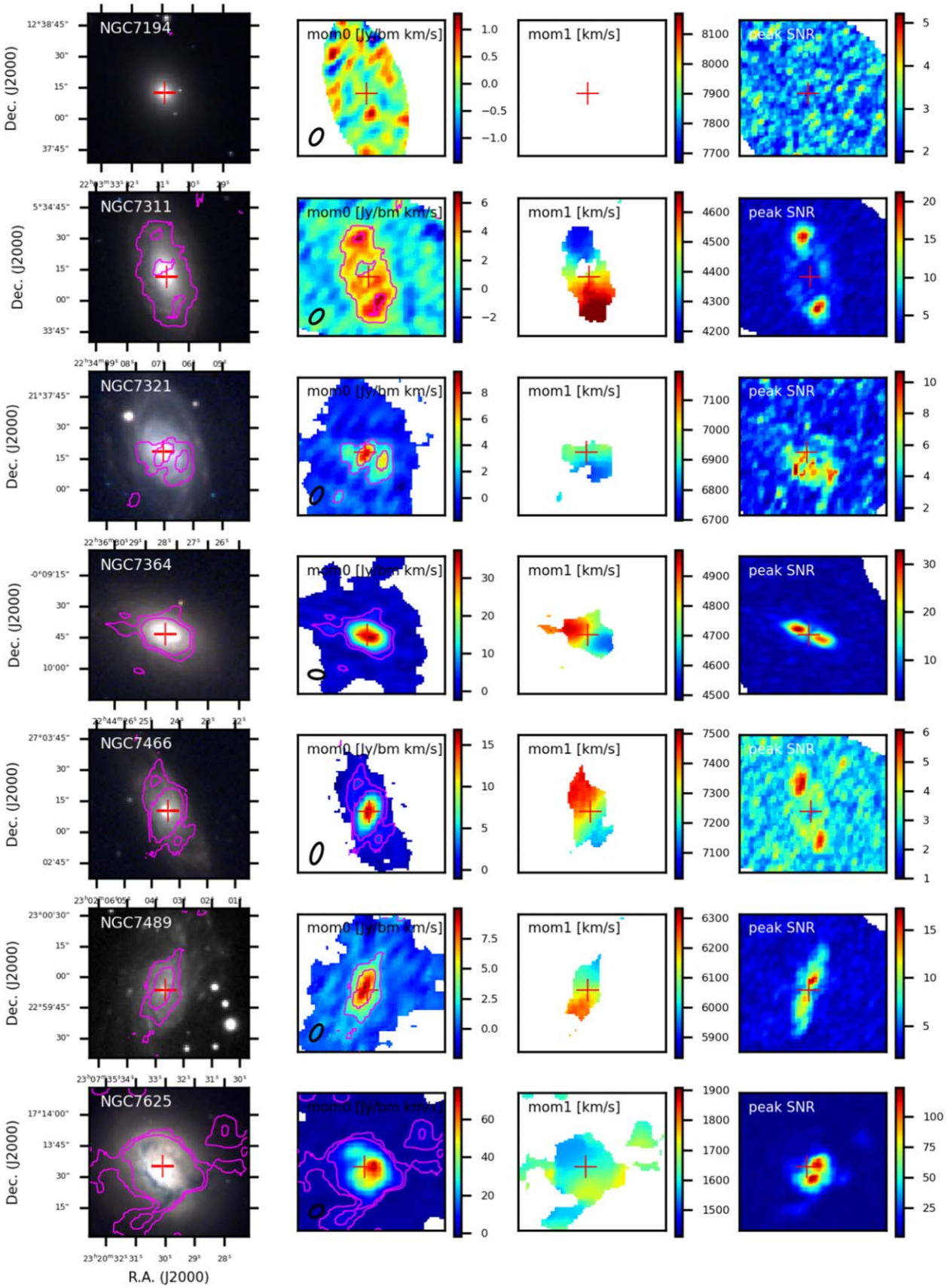

Figure 18. Images for ACA EDGE galaxies. See caption of Figure 3.

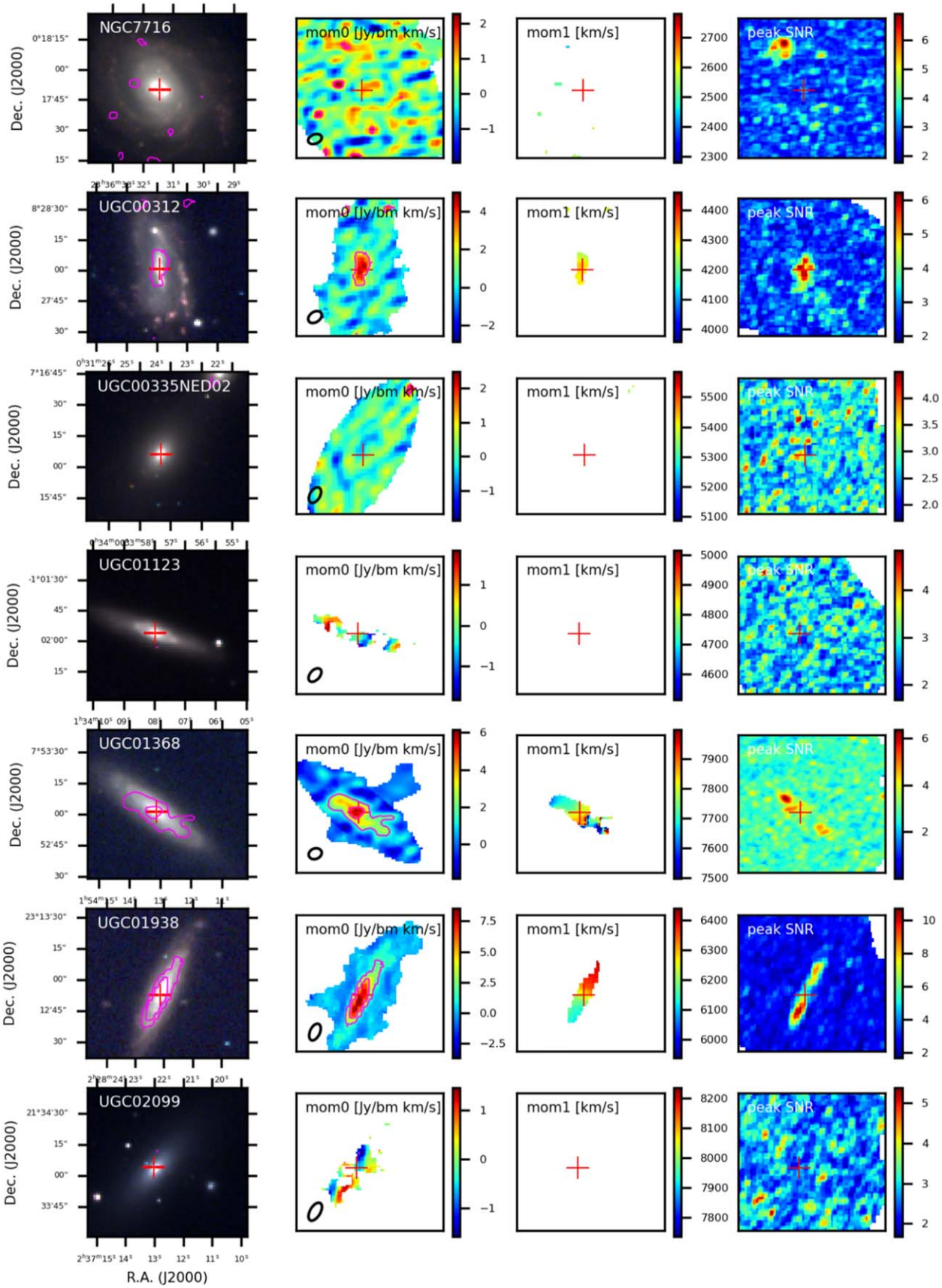

Figure 19. Images for ACA EDGE galaxies. See caption of Figure 3.

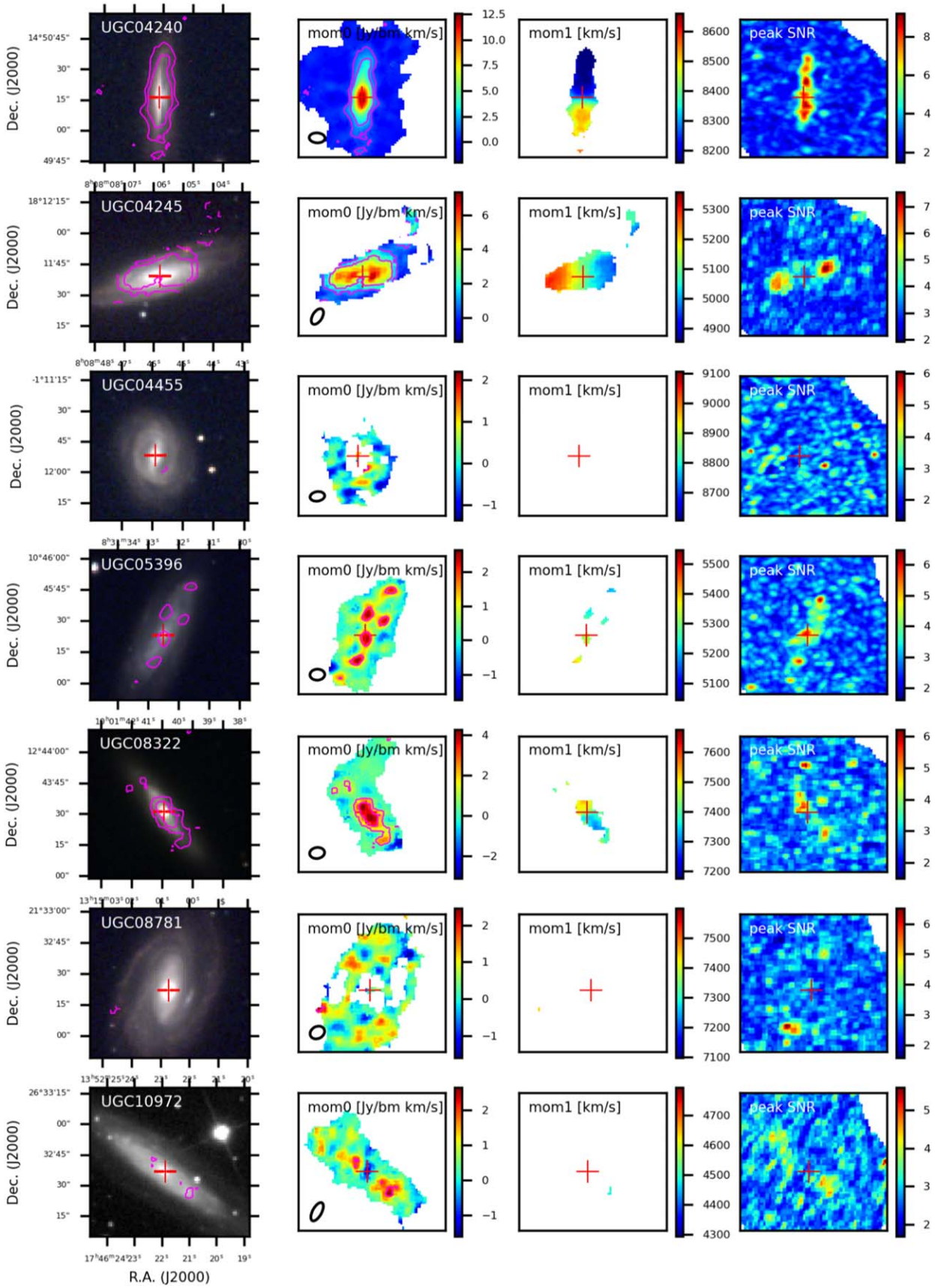

Figure 20. Images for ACA EDGE galaxies. See caption of Figure 3.

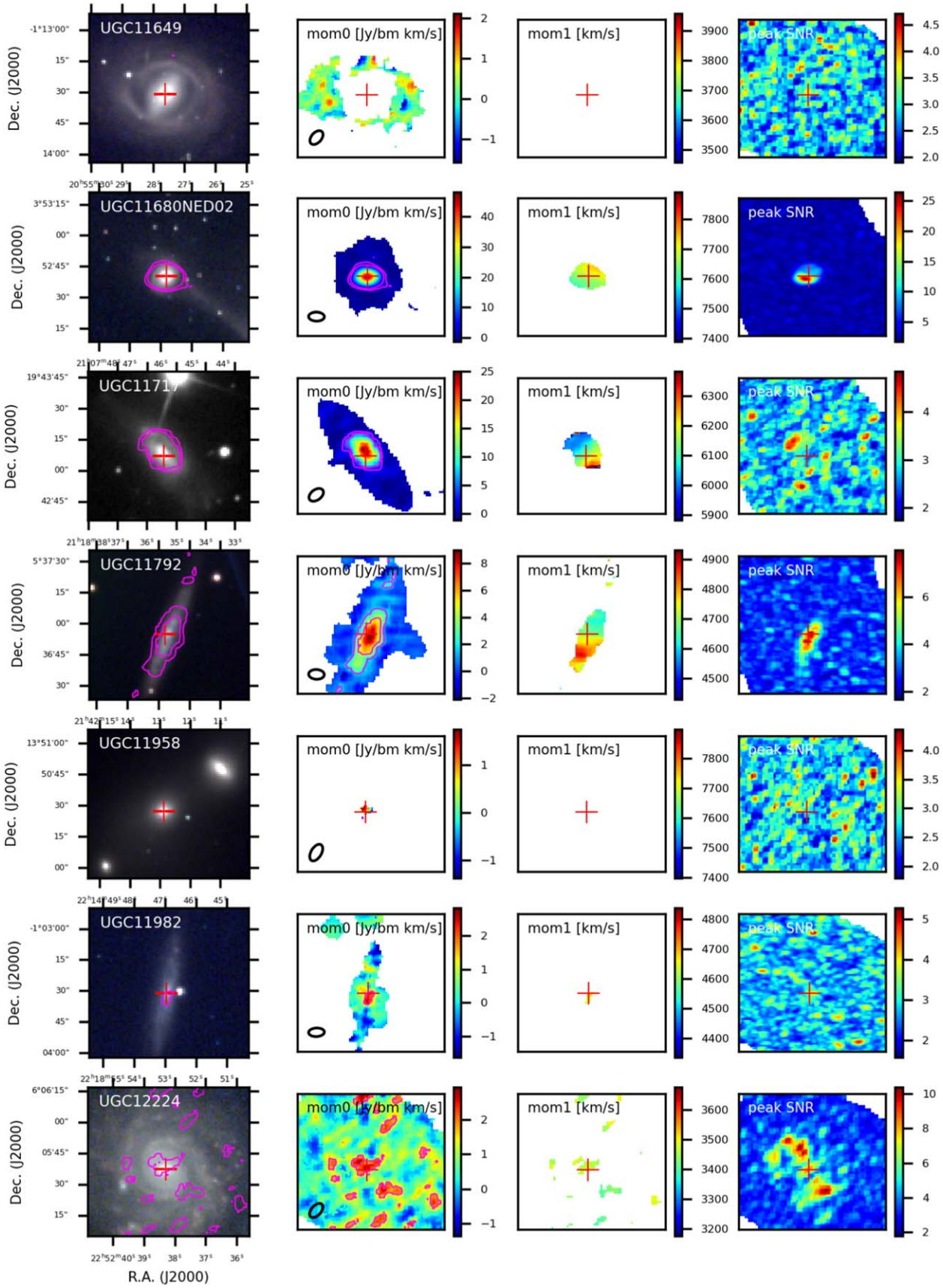

Figure 21. Images for ACA EDGE galaxies. See caption of Figure 3.

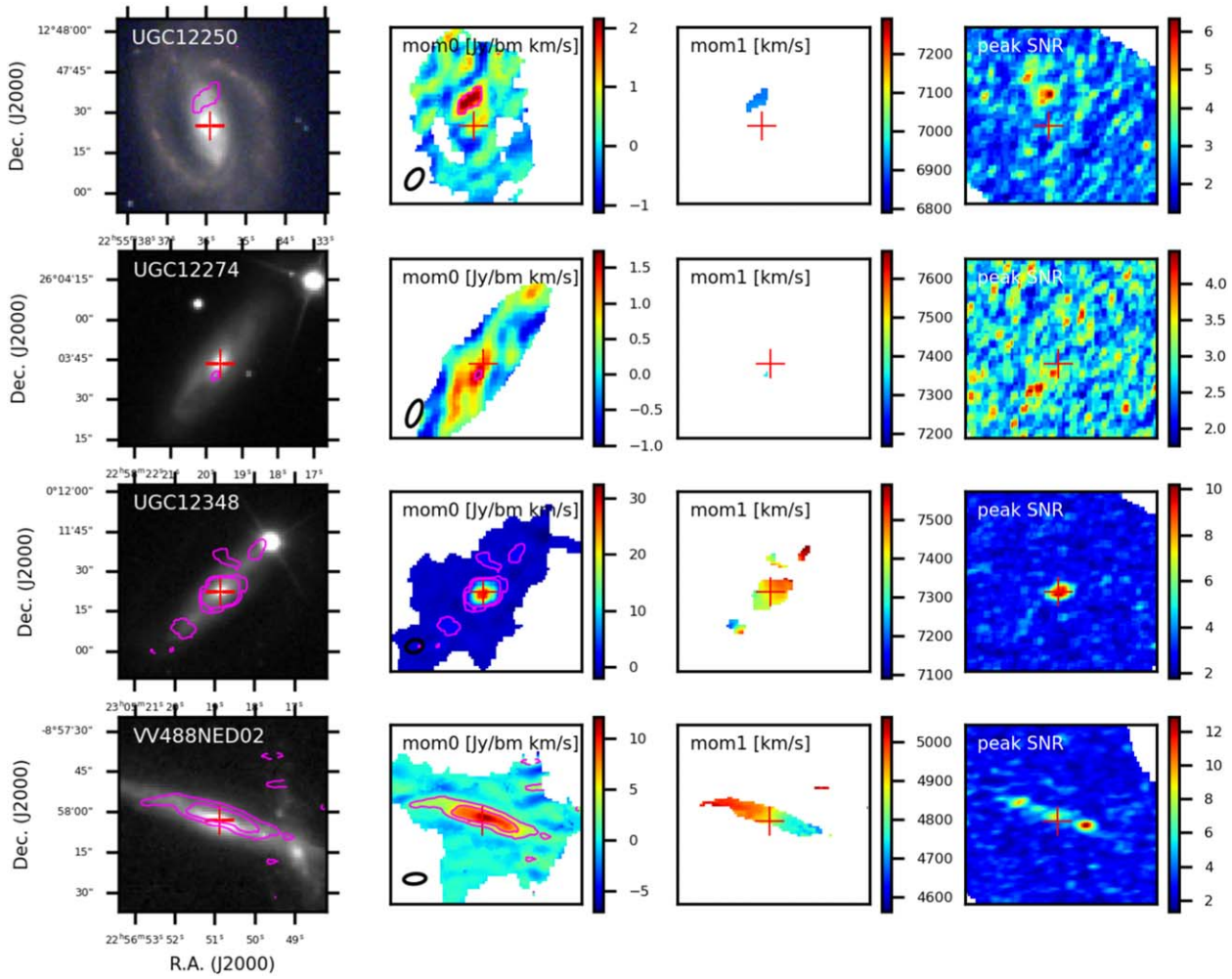

Figure 22. Images for ACA EDGE galaxies. See caption of Figure 3.

ORCID iDs

Vicente Villanueva https://orcid.org/0000-0002-5877-379X
Alberto D. Bolatto https://orcid.org/0000-0002-5480-5686
Stuart N. Vogel https://orcid.org/0000-0002-8765-7915
Tony Wong https://orcid.org/0000-0002-7759-0585
Adam K. Leroy https://orcid.org/0000-0002-2545-1700
Sebastian F. Sánchez https://orcid.org/0000-0001-6444-9307
Rebecca C. Levy https://orcid.org/0000-0003-2508-2586
Erik Rosolowsky https://orcid.org/0000-0002-5204-2259
Dario Colombo https://orcid.org/0000-0001-6498-2945
Veselina Kalinova https://orcid.org/0000-0002-2262-5875
Serena Cronin https://orcid.org/0000-0002-9511-1330
Peter Teuben https://orcid.org/0000-0003-1774-3436

References

Alam, S., Albareti, F. D., Allende Prieto, C., et al. 2015, ApJS, 219, 12
Astropy Collaboration, Price-Whelan, A. M., Sipőcz, B. M., et al. 2018, AJ, 156, 123
Balogh, M. L., & Morris, S. L. 2000, MNRAS, 318, 703
Baumgartner, W. H., & Mushotzky, R. F. 2006, ApJ, 639, 929
Belfiore, F., Maiolino, R., Maraston, C., et al. 2016, MNRAS, 461, 3111
Bigiel, F., Leroy, A., Walter, F., et al. 2008, AJ, 136, 2846
Bland-Hawthorn, J., & Gerhard, O. 2016, ARA&A, 54, 529
Bluck, A. F. L., Maiolino, R., Piotrowska, J. M., et al. 2020a, MNRAS, 499, 230
Bluck, A. F. L., Maiolino, R., Sánchez, S. F., et al. 2020b, MNRAS, 492, 96
Bolatto, A. D., Wolfire, M., & Leroy, A. K. 2013, ARA&A, 51, 207
Bolatto, A. D., Wong, T., Utomo, D., et al. 2017, ApJ, 846, 159
Boselli, A., Ciesla, L., Buat, V., et al. 2010, A&A, 518, L61
Boselli, A., Cortese, L., & Boquien, M. 2014, A&A, 564, A65
Bottinelli, L., Gouguenheim, L., Fouque, P., & Paturel, G. 1990, A&AS, 82, 391
Bottinelli, L., Gouguenheim, L., & Paturel, G. 1982, A&AS, 47, 171
Briggs, D. S. 1995, PhD thesis, New Mexico Institute of Mining and Technology
Brinchmann, J., Charlot, S., White, S. D. M., et al. 2004, MNRAS, 351, 1151
Brown, T., Wilson, C. D., Zabel, N., et al. 2021, ApJS, 257, 21
Brownson, S., Belfiore, F., Maiolino, R., Lin, L., & Carniani, S. 2020, MNRAS, 498, L66
Cano-Díaz, M., Sánchez, S. F., Zibetti, S., et al. 2016, ApJL, 821, L26
Cardelli, J. A., Clayton, G. C., & Mathis, J. S. 1989, ApJ, 345, 245
CASA Team, Bean, B., Bhatnagar, S., et al. 2022, PASP, 134, 114501
Catalán-Torrecilla, C., Gil de Paz, A., Castillo-Morales, A., et al. 2017, ApJ, 848, 87
Chang, Y.-Y., van der Wel, A., da Cunha, E., & Rix, H.-W. 2015, ApJS, 219, 8
Colombo, D., Kalinova, V., Utomo, D., et al. 2018, MNRAS, 475, 1791
Colombo, D., Sanchez, S. F., Bolatto, A. D., et al. 2020, A&A, 644, A97
Cook, R. H. W., Cortese, L., Catinella, B., & Robotham, A. 2019, MNRAS, 490, 4060
Cook, R. H. W., Cortese, L., Catinella, B., & Robotham, A. 2020, MNRAS, 493, 5596
Corcho-Caballero, P., Ascasibar, Y., Sánchez, S. F., & López-Sánchez, Á. R. 2023, MNRAS, 520, 193
Daddi, E., Dickinson, M., Morrison, G., et al. 2007, ApJ, 670, 156
de Vaucouleurs, G., de Vaucouleurs, A., Corwin, H. G., Jr., et al. 1991, S&T, 82, 621

den Brok, J. S., Chatzigiannakis, D., Bigiel, F., et al. 2021, MNRAS, 504, 3221
Eales, S., Eales, O., & de Vis, P. 2020, MNRAS, 491, 69
Ellison, S. L., Brown, T., Catinella, B., & Cortese, L. 2019, MNRAS, 482, 5694
Ellison, S. L., Lin, L., Thorp, M. D., et al. 2021a, MNRAS, 501, 4777
Ellison, S. L., Sánchez, S. F., Ibarra-Medel, H., et al. 2018, MNRAS, 474, 2039
Ellison, S. L., Teimoorinia, H., Rosario, D. J., & Mendel, J. T. 2016, MNRAS, 458, L34
Ellison, S. L., Wong, T., Sánchez, S. F., et al. 2021b, MNRAS, 505, L46
Esposito, F., Vallini, L., Pozzi, F., et al. 2022, MNRAS, 512, 686
Fabello, S., Kauffmann, G., Catinella, B., et al. 2011, MNRAS, 416, 1739
García-Lorenzo, B., Márquez, I., Barrera-Ballesteros, J. K., et al. 2015, A&A, 573, A59
Gensior, J., & Kruijssen, J. M. D. 2021, MNRAS, 500, 2000
Gensior, J., Kruijssen, J. M. D., & Keller, B. W. 2020, MNRAS, 495, 199
Gunn, J. E., & Gott, J. R. I. 1972, ApJ, 176, 1
Harris, C. R., Millman, K. J., van der Walt, S. J., et al. 2020, Natur, 585, 357
Ho, L. C., Darling, J., & Greene, J. E. 2008, ApJ, 681, 128
Hunter, J. D. 2007, CSE, 9, 90
Hunter, T. R., Indebetouw, R., Brogan, C. L., et al. 2023, PASP, 135, 074501
Husemann, B., Wisotzki, L., Sánchez, S. F., & Jahnke, K. 2008, A&A, 488, 145
Jiménez-Donaire, M. J., Brown, T., Wilson, C. D., et al. 2023, A&A, 671, A3
Kalinova, V., Colombo, D., Sánchez, S. F., et al. 2021, A&A, 648, A64
Kalinova, V., Colombo, D., Sánchez, S. F., et al. 2022, A&A, 665, A90
Kawata, D., & Mulchaey, J. S. 2008, ApJL, 672, L103
Kewley, L. J., Dopita, M. A., Sutherland, R. S., Heisler, C. A., & Trevena, J. 2001, ApJ, 556, 121
Koss, M. J., Strittmatter, B., Lamperti, I., et al. 2021, ApJS, 252, 29
Lacerda, E. A. D., Sánchez, S. F., Cid Fernandes, R., et al. 2020, MNRAS, 492, 3073
Larson, R. B., Tinsley, B. M., & Caldwell, C. N. 1980, ApJ, 237, 692
Leroy, A. K., Hughes, A., Liu, D., et al. 2021a, ApJS, 255, 19
Leroy, A. K., Schinnerer, E., Hughes, A., et al. 2021b, ApJS, 257, 43
Leroy, A. K., Walter, F., Brinks, E., et al. 2008, AJ, 136, 2782
Leroy, A. K., Walter, F., Sandstrom, K., et al. 2013, AJ, 146, 19
Levy, R. C., Bolatto, A. D., Teuben, P., et al. 2018, ApJ, 860, 92
Lin, L., Ellison, S. L., Pan, H.-A., et al. 2020, ApJ, 903, 145
Lin, L., Ellison, S. L., Pan, H.-A., et al. 2022, ApJ, 926, 175
Lin, L., Pan, H.-A., Ellison, S. L., et al. 2019, ApJL, 884, L33
Maiolino, R., Ruiz, M., Rieke, G. H., & Papadopoulos, P. 1997, ApJ, 485, 552
Marino, R. A., Rosales-Ortega, F. F., Sánchez, S. F., et al. 2013, A&A, 559, A114
Martig, M., Bournaud, F., Teyssier, R., & Dekel, A. 2009, ApJ, 707, 250
Martig, M., Crocker, A. F., Bournaud, F., et al. 2013, MNRAS, 432, 1914
Mendel, J. T., Simard, L., Palmer, M., Ellison, S. L., & Patton, D. R. 2013, ApJS, 210, 3
Méndez-Abreu, J., Aguerri, J. A. L., Corsini, E. M., & Simonneau, E. 2008, arXiv:0802.0010
Méndez-Abreu, J., Debattista, V. P., Corsini, E. M., & Aguerri, J. A. L. 2014, A&A, 572, A25
Méndez-Abreu, J., Ruiz-Lara, T., Sánchez-Menguiano, L., et al. 2017, A&A, 598, A32
Moore, B., Katz, N., Lake, G., Dressler, A., & Oemler, A. 1996, Natur, 379, 613
Nesvadba, N. P. H., Polletta, M., Lehnert, M. D., et al. 2011, MNRAS, 415, 2359
Oppenheimer, B. D., Davé, R., Kereš, D., et al. 2010, MNRAS, 406, 2325
Page, M. J., Symeonidis, M., Vieira, J. D., et al. 2012, Natur, 485, 213
Pedregosa, F., Varoquaux, G., Gramfort, A., et al. 2011, JMLR, 12, 2825
Peng, Y., Maiolino, R., & Cochrane, R. 2015, Natur, 521, 192
Peng, Y.-j., Lilly, S. J., Kovač, K., et al. 2010, ApJ, 721, 193
Pessa, I., Schinnerer, E., Belfiore, F., et al. 2021, A&A, 650, A134
Querejeta, M., Schinnerer, E., Meidt, S., et al. 2021, A&A, 656, A133
Regan, M. W., Thornley, M. D., Helfer, T. T., et al. 2001, ApJ, 561, 218
Rosa-González, D., Terlevich, E., & Terlevich, R. 2002, MNRAS, 332, 283
Rosolowsky, E., & Leroy, A. 2006, PASP, 118, 590
Roth, M. M., Kelz, A., Fechner, T., et al. 2005, PASP, 117, 620
Saintonge, A., Catinella, B., Cortese, L., et al. 2016, MNRAS, 462, 1749
Saintonge, A., Catinella, B., Tacconi, L. J., et al. 2017, ApJS, 233, 22
Saintonge, A., Kauffmann, G., Kramer, C., et al. 2011, MNRAS, 415, 32
Salim, S., Rich, R. M., Charlot, S., et al. 2007, ApJS, 173, 267
Sánchez, S. F. 2020, ARA&A, 58, 99
Sánchez, S. F., Avila-Reese, V., Hernandez-Toledo, H., et al. 2018, RMxAA, 54, 217
Sánchez, S. F., Barrera-Ballesteros, J. K., Colombo, D., et al. 2021c, MNRAS, 503, 1615
Sánchez, S. F., Barrera-Ballesteros, J. K., Sánchez-Menguiano, L., et al. 2017, MNRAS, 469, 2121
Sánchez, S. F., García-Benito, R., Zibetti, S., et al. 2016a, A&A, 594, A36
Sánchez, S. F., Gómez Medina, D. C., Barrera-Ballesteros, J. K., et al. 2023, in IAU Symp. 373, Resolving the Rise and Fall of Star Formation in Galaxies (Cambridge: Cambridge Univ. Press), 3
Sánchez, S. F., Kennicutt, R. C., Gil de Paz, A., et al. 2012, A&A, 538, A8
Sánchez, S. F., Pérez, E., Sánchez-Blázquez, P., et al. 2016b, RMxAA, 52, 21
Sánchez, S. F., Pérez, E., Sánchez-Blázquez, P., et al. 2016c, RMxAA, 52, 171
Sánchez, S. F., Walcher, C. J., Lopez-Cobá, C., et al. 2021, RMxAA, 57, 3
Schawinski, K., Urry, C. M., Simmons, B. D., et al. 2014, MNRAS, 440, 889
Schruba, A., Leroy, A. K., Walter, F., et al. 2011, AJ, 142, 37
Sersic, J. L. 1968, Atlas de Galaxias Australes (Cordoba: Observatorio Astronomico)
Simard, L., Mendel, J. T., Patton, D. R., Ellison, S. L., & McConnachie, A. W. 2011, ApJS, 196, 11
Simard, L., Willmer, C. N. A., Vogt, N. P., et al. 2002, ApJS, 142, 1
Singh, R., van de Ven, G., Jahnke, K., et al. 2013, A&A, 558, A43
Smith, R., Davies, J. I., & Nelson, A. H. 2010, MNRAS, 405, 1723
Speagle, J. S., Steinhardt, C. L., Capak, P. L., & Silverman, J. D. 2014, ApJS, 214, 15
Sun, J., Leroy, A. K., Ostriker, E. C., et al. 2023, ApJL, 945, L19
Toomre, A. 1964, ApJ, 139, 1217
Veilleux, S., Shopbell, P. L., Rupke, D. S., Bland-Hawthorn, J., & Cecil, G. 2003, AJ, 126, 2185
Villanueva, V., Bolatto, A., Vogel, S., et al. 2021, ApJ, 923, 60
Villanueva, V., Bolatto, A. D., Vogel, S., et al. 2022, ApJ, 940, 176
Virtanen, P., Gommers, R., Oliphant, T. E., et al. 2020, NatMe, 17, 261
Vollmer, B., & Davies, R. I. 2013, A&A, 556, A31
Walcher, C. J., Wisotzki, L., Bekeraité, S., et al. 2014, A&A, 569, A1
Walter, F., Brinks, E., de Blok, W. J. G., et al. 2008, AJ, 136, 2563
Waskom, M. L. 2021, JOSS, 6, 3021
Whitaker, K. E., van Dokkum, P. G., Brammer, G., & Franx, M. 2012, ApJL, 754, L29
Wilson, C. D., Warren, B. E., Israel, F. P., et al. 2012, MNRAS, 424, 3050
York, D. G., Adelman, J., Anderson, J. E., Jr., et al. 2000, AJ, 120, 1579
Young, J. S., Xie, S., Tacconi, L., et al. 1995, ApJS, 98, 219
Zabel, N., Brown, T., Wilson, C. D., et al. 2022, ApJ, 933, 10